## Department of Precision and Microsystems Engineering

# Guiding, splitting and interference of high-frequency Lamb waves in gold-coated SiN membranes with phononic crystal structures

Jikke van Hernen

| | |
|---|---|
| Report no | : 2025.060 |
| Coach | : Dr. R.H. Guis |
| Professors | : Dr. G.J. Verbiest & Dr. R.A. Norte |
| Specialisation | : DNM |
| Type of report | : MSc Thesis |
| Date | : September 9, 2025 |

Challenge the future

Delft University of Technology
MSc Thesis
Department of Precision and Microsystems Engineering

# Guiding, splitting and interference of high-frequency Lamb waves in gold-coated SiN membranes with phononic crystal structures

*Author:*
Jikke van Hernen

*Supervisors:*
Dr. G.J. Verbiest
Dr. R.A. Norte

*Mentor:*
Dr. R.H. Guis

September 9, 2025

## Acknowledgments

I would like to express my sincere gratitude to my supervisors, **Gerard Verbiest** and **Richard Norte**, for their excellent guidance, support, and insightful discussions throughout this thesis. The (almost) weekly meetings with both of you drastically increased my knowledge on photoacoustics and helped to keep momentum in this project.

A special thanks to **Ruben Guis**, for building such a complex setup and trusting me to use it. You made sure that setup was always functioning and available. Your knowledge on photoacoustics, the setup and the software made the experimental work much smoother and more efficient.

I would also like to thank **Bart Langen** for making the time in the lab even more enjoyable. Finally, I am also grateful for **Joop Andriesse** and **Sola Olokun** for keeping me company during the summer break while we worked on our theses.

# Abstract

In this thesis, a femtosecond pump-probe laser setup is used to study GHz acoustic waves in suspended phononic crystal (PnC) waveguides. These membranes consist of 200 nm thick $Si_3N_4$ coated with a 20 nm gold film and shamrock shaped PnCs. Various COMSOL simulations of these waveguides are conducted to investigate the expected behavior of the membranes. These simulations not only reveal the eigenmodes and phononic bandgaps of two different membranes, but also show the formation of a 300 MHz Lamb wave inside the waveguide. Experimental results show that this 300 MHz Lamb wave is confined inside the waveguide, when the frequency of the Lamb wave falls within the phononic bandgap of the membrane. For membranes with a bandgap that does not include the frequency of the Lamb wave, propagation through the PnC lattice is seen. Finally, an Acousto-Optic Modulator (AOM) is successfully integrated in the pump-probe laser setup to increase the frequency resolution of the measurements. The experimental data obtained with this higher frequency resolution shows similar results of wave confinement and proves repeatability of the measurements.

# Contents

# 1 Introduction

Photonic integrated circuits (PICs) are widely used for numerous applications, like sensing, high speed telecommunications, high performance computing, quantum technologies and much more. This has led to rapid development of these PICs [1]. In the last years, the acoustic counterparts of PICs have received more and more attention. This is because phononic integrated circuits (PnICs) may be the solution to reduce the size of signal processing devices drastically, as GHz sound waves have a factor $10^5$ smaller wavelength than EM waves at the same frequency [2]. Acoustic waves also show lower signal interference and lower losses than electromagnetic waves. [3]. Sensors based on phononic waveguides can have a big impact on the field of bio, medical and chemical sensing, since the absence of electric components at the point of measuring allow for usage in rough environments [4].

These PnICs consist of elements like interdigitated transducers (IDTs), ring resonators and phononic waveguides. The IDTs are able to convert the signals to phonons at the inlet of the PnIC and convert it back to a signal at the outlet of the PnIC. The ring resonators allow for narrow band signal filtration, phonon memory and improvement of the phonon-matter interaction. To transport the acoustic waves from one component to another through this PnIC, phononic waveguides come in to play. Before the complex PnICs can be implemented, these single components have to be researched and tested extensively. Experimental PnICs show the need to split the waveguide, and thus the acoustic waves, in multiple directions [5]. In addition to this, the phononic waveguides should exhibit low energy loss. This is important because the PnICs are larger than the single phononic waveguide. If the acoustic wave loses most of its energy in the waveguide, detecting it near the end of the PnICs would become challenging [6].

Currently, the operation frequencies of wireless communication are in the range of 1 GHz. Future operation frequencies of this wireless communication are predicted to reach up to hundreds of GHz. With PnC waveguides being a potential candidate for the new-gen signal processing devices of wireless communication, it is required that the PnC waveguides can operate in the hypersonic ( $>$ 1 GHz) regime. Only then can they be used as hypersonic bulk acoustic wave (BAW), surface acoustic wave (SAW) and Lamb wave filters [7].

In the MSc thesis of M. van der Vis [8], a knowledge gap is addressed regarding the splitting of acoustic waves. In literature there are no examples to be found that realize on-chip beam splitting, which is needed for the progression of PnICs. After an extensive literature review, a design of a suspended gold coated $Si_3N_4$ acoustic beam splitter phononic crystals (PnCs) consisting of air is introduced, followed by simulations with GHz waves. This work is followed up by the Msc thesis of A. Soltész [9], where the design of the acoustic beam splitters is optimized and numerically validated. After validation, multiple configurations were manufactured and a first experiment was realized.

The main objective of this MSc thesis is to show efficient confinement of Lamb waves in the waveguides that were manufactured by A. Soltész. To do this, data of the Lamb waves generated at the inlet of the waveguide will be compared with the data at various locations in the waveguide. This experimental data will form be the foundation for answering the research question: "How do different configurations of suspended SiN membranes with Shamrock shaped air PnCs perform in confining out-of-plane acoustic waves on-chip?" This research question will be answered by discussing the fundamental principles needed for acoustic waveguides and state-of-the-art research in Chapter 2. In Chapter 3, the experimental plan and materials used to test the waveguides are discussed. Chapter 4 presents the results obtained during this thesis. The obtained results are discussed in Chapter 5 and the conclusions of this thesis are presented in Chapter 6.

To perform the experiments, a femtosecond laser pump-probe setup has been made available at TU Delft [10]. This setup uses a pump laser that emits 100 mW laser pulses with a duration of 100 fs to create the acoustic waves on the surface of the sample. These acoustic waves are measured by the probe laser that is delay with respect to the pump laser and uses laser pulses of around 5-7 mW with the same duration as the pump laser. The setup presented in the study has been improved by adding a balanced photodetector to increase the sensitivity.

In addition, an L-shaped mask with two pinholes in it has been added to the path of the pump laser. The trimmed coherent light beams that pass through the pinholes create an interference pattern on the sample. Varying the distance between the pinholes or the diameter of the pinholes results in different spacing between the bright and dark fringes of the interference pattern. The spacing of the interference pattern is then related to the frequency of the acoustic waves, making it possible to tune this frequency [9].

To validate the acoustic beam splitters, acoustic waves will be excited at the inlet of the waveguide. At this point, the acoustic modes present in the suspended waveguide can be identified. After identifying the mode that is desired to guide, the position of the probe can be varied. If the position of the probe is moved along waveguide, the movement of the mode through the waveguide can be reconstructed. Measuring inside the PnC lattice should confirm the absence of the mode, indicating it is confined to the waveguide. By comparing the amplitude of the desired mode at different locations within the waveguide, the energy loss to the substrate can be monitored.

# 2 Theoretical Background

This section provides an overview of PnC acoustic waveguides and the fundamental principles governing acoustic wave propagation within them. It starts by outlining the theory of PnCs, the bandgap of these PnCs and confinement mechanisms. Following this, the physical concepts like wave modes, wave generation and wave detection of acoustic waves are presented. Finally, an overview of relevant literature and state-of-the-art techniques is included to contextualize the development of acoustic waveguiding.

## 2.1 Acoustic Waveguides

Phononic crystals (PnCs) are artificial periodic structures included into a homogeneous material that block acoustic wave propagation within a certain frequency range. This means that traveling waves within this frequency range can not propagate through the lattice of these crystals. The range of frequencies that is blocked by the PnC lattice, is the so-called bandgap [11] [12]. Waveguides can be created by removing certain PnCs from the periodic lattice, forming paths to guide and bend the acoustic waves. If the frequency of these waves is within the band gap of the crystal, they will be confined to the created paths as the wave can not propagate into the crystal lattice. Figure 1 shows three examples with different paths to guide the acoustic waves [13].

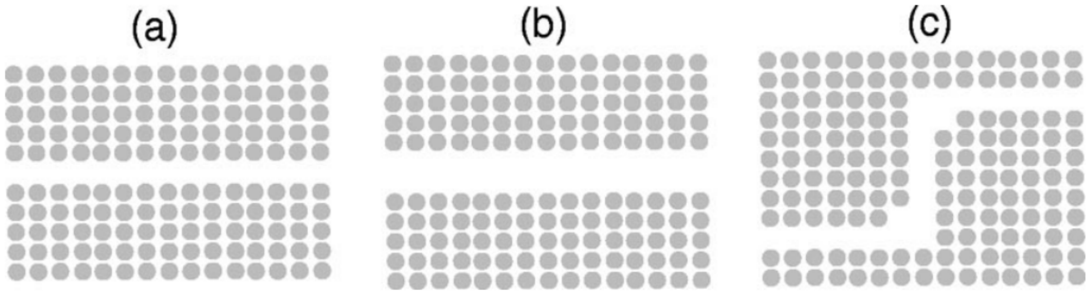

**Figure 1.** Different paths in waveguides composed of steel rods immersed in water. **a)** Straight waveguide formed by the removal of a single row of steel rods. **b)** Straight waveguide formed by the removal of two rows of steel rods. **C)** S-shaped waveguide [13].

The characteristics of a PnC, like shape, size or material, give rise to different band diagrams. Each band diagram has a specific band gap, where incident waves of frequencies inside this band gap are prohibited to propagate [14]. As an example, Figure 2 shows the band diagram of circular air holes. Here the band gap is indicated in gray and is centered around 3.40 GHz.

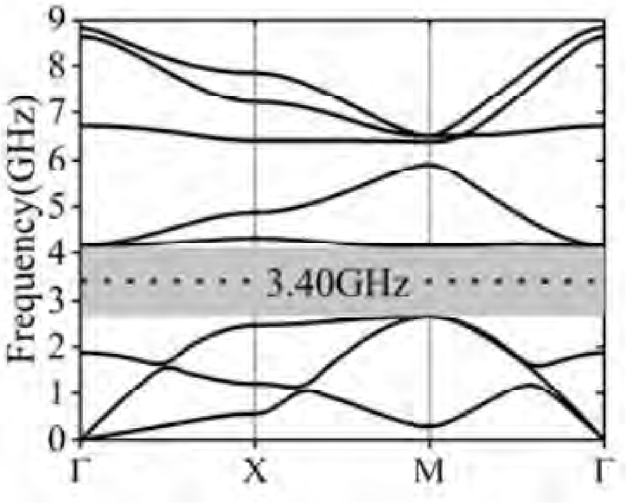

**Figure 2.** Example of a band diagram formed by PnCs that are circular air holes with a diameter of 190 nm. The phononic bandgap is centered around 3.40 GHz and is indicated in grey [14].

The mid frequency of the band gap, 3.40 GHz in the example above, is not the only relevant parameter. The bandwidth of the band gap allows for a broader range of frequencies to be blocked by the PnC lattice. This means that acoustic waves with a deviating frequency are still confined in the waveguide. By varying the characteristics of the PnCs, a band gap with the desired mid frequency and bandwidth can be created to confine acoustic waves in the waveguide.

One of the mechanisms that contributes to the formation of a bandgap, is the presence of Bragg gaps. These Bragg gaps are mainly caused by the periodic inclusion of PnCs, like in the waveguide. Incident waves of certain frequencies experience destructive interference when they are scattered from the PnC. The range of frequencies for which this destructive interference occurs, is the bandgap that forms [15]. The wavelength at which these Bragg gaps generally emerge are usually in the same order as the spacing between these period inclusions [16]. The other effect that can result in band gaps occurs primarily due to the resonance characteristics of the individual cells within the crystal. These types of band gaps are seen at low frequencies (in the order of 100 Hz) [17]. As the goal is to guide GHz waves, the Bragg band gaps are most relevant since these can form in the GHz regime.

## 2.2 Fundamentals of Acoustic Waves

There are three different type of acoustic waves that may be propagate in the waveguides: Bulk Acoustic Waves (BAWs), Surface Acoustic Waves (SAWs) and Lamb waves. The main characteristics of these waves are discussed first in this subsection. After this, two different techniques of generating acoustic waves are investigated.

### 2.2.1 Acoustic Wave Types

The acoustic waves that are generated in the suspended membranes can be of different origin. Most common, there are three types of waves considered: bulk acoustic waves (BAWs), surface acoustic waves (SAWs) and Lamb waves. BAWs are waves that are spread into the bulk of the sample and can be either longitudinal or transverse. SAWs on the other hand, are confined only to the surface of the sample and propagate along the direction of the surface. The two types of SAWs are Rayleigh waves and Love waves. Lamb waves propagate in plate-like structures and are generally observed when:

$$d \leq \lambda \tag{1}$$

where $d$ is the thickness of the plate and $\lambda$ is the wavelength of the Lamb wave [18]. These Lamb waves can be seen as two Rayleigh waves on the top and bottom surface of the membrane. [19]. Figure 3 visualizes the types of waves discussed above.

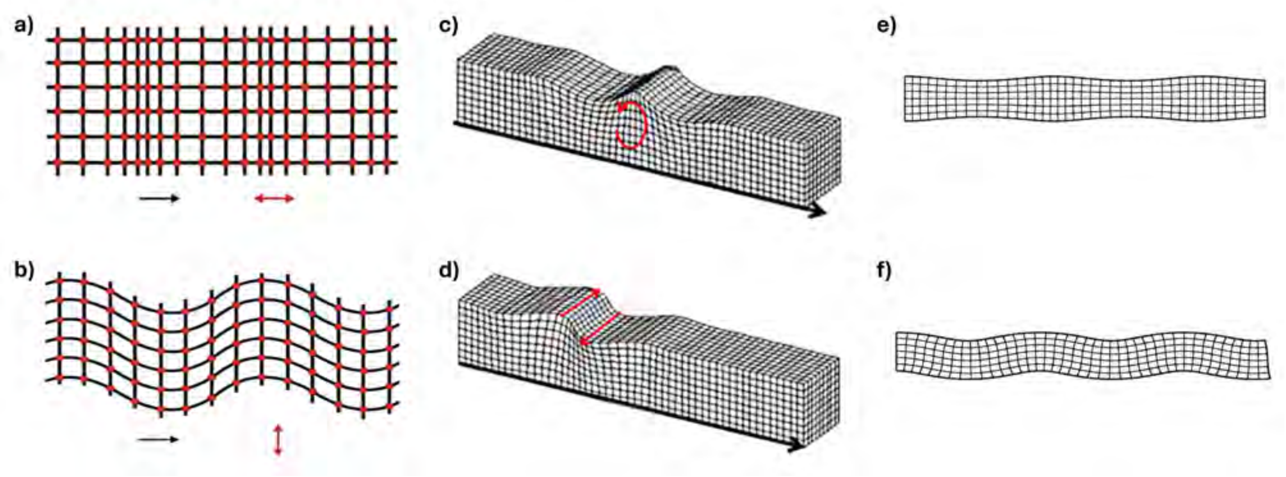

**Figure 3.** Common wave types found in acoustic waveguides. **a)** Longitudinal BAW. **b)** Transverse BAW. **c)** Rayleigh SAW. **d)** Love SAW. **e)** Symmetric Lamb wave. **f)** Asymmetric Lamb wave [20] [21] [22].

In his MSc thesis, A. Soltész stated the presence of BAWs, SAWs and Lamb waves in the suspended waveguide. The BAW was observed to repeatedly travel from top to bottom of the gold coating at the point where the pump laser is focused. Furthermore, this BAW can only be observed for a short time (3 ns), as it quickly decays. A SAW was found to be caused by the spot size of the laser and traveled along the surface of the gold layer. This SAW had almost completely decayed at 50 $\mu$m from the pump laser. Lastly, an asymmetric Lamb wave traveling along the membrane was identified. Unlike the SAW, this Lamb wave was still observed at 100 $\mu$m from the pump laser [9]. This indicates a lower energy loss to the substrate, potentially making this Lamb wave better for guiding and splitting than the SAW.

### 2.2.2 Acoustic Wave Generation

A common technique to initiate surface acoustic waves is by using interdigitated transducers (IDTs). These IDTs are comb like structures that are patterned on top of a piezoelectric substrate. The wavelength, $\lambda$, of the resulting SAW is equal to the distance between two fingers of the IDT of the same polarity (i.e. twice the distance between two adjacent fingers) [23]. A schematic of an arbitrary IDT can be seen in Figure 4.

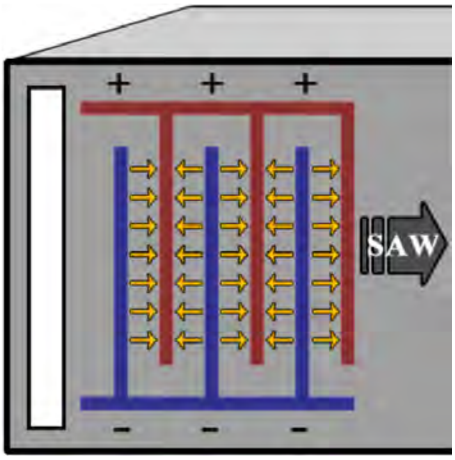

**Figure 4.** Schematic of an IDT on top of a piezoelectric substrate [24].

To establish the acoustic waves, an alternating current (AC) is applied to the IDTs. The alternation of this current results in positive and negative electric fields, that alternate simultaneously. This alternating electric field induces local compression and tension in the substrate between the fingers due to the piezoelectric properties. This tension and compression launches a SAW along the surface of the substrate. The downside of the acoustic waves generated by this process, is that the SAW propagates from both sides of the IDT (Figure 4 only shows one SAW, as the SAW propagating to the left is blocked by the white bar). This means that the acoustic waves entering the waveguide will only have half of the energy of the generated wave [24]. This loss of energy can be mitigated by using different configurations of IDTs.

Another process that can create acoustic waves in a material, is through excitation of the electrons with a laser pulse. For the case of metals, electrons in the conduction band are excited to higher, non-equilibrium states by absorbing the electromagnetic energy of the laser through photon-electron interaction. These non equilibrium electrons transfer their energy to the lattice through electron-phonon coupling, this process is in the order of tens of picoseconds. The energy transfer to the lattice results in an increase of temperature of the lattice [25]. The dynamics of how this energy is transferred is described by the empirical two-temperature model (TTM) [26]. The 1D-TTM is governed by the following equations:

$$\begin{aligned} C_e\frac{\partial T_e}{\partial t} &= \frac{\partial}{\partial z}\left(k_e\frac{\partial T_e}{\partial z}\right) - G_{eL}(T_e - T_L) + S \\ C_L\frac{\partial T_L}{\partial t} &= \frac{\partial}{\partial z}\left(k_L\frac{\partial T_L}{\partial z}\right) + G_{eL}(T_e - T_L) \end{aligned} \tag{2}$$

where the temperature of the electron and the lattice are given by $T_e$ and $T_L$ respectively. The metal that is used for the film, like gold, determines the following parameters: volumetric heat capacity for the electron ($C_e$) and the lattice ($C_L$), heat conductivity for the electron ($k_e$) and the lattice ($k_L$), the electron-phonon coupling strength $G_{eL}$ . Finally, the laser energy absorbed by the electrons is accounted for in the source term, denoted by $S$. The evolution of the electron and lattice temperature predicted by this TTM is shown in Figure 5 for gold films of various thicknesses [27].

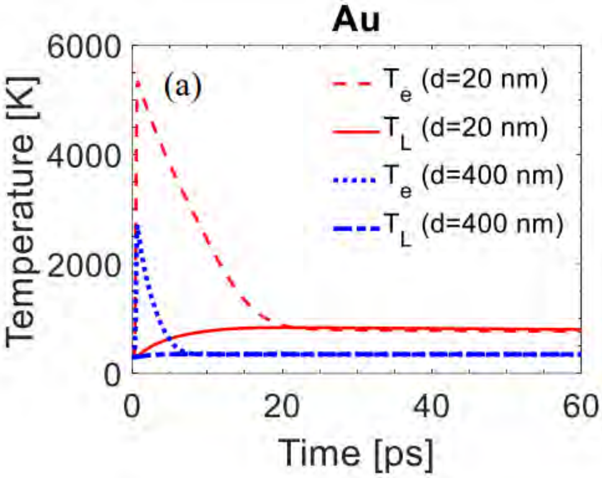

**Figure 5.** Evolution of electron and lattice temperature for a 20 nm and 200 nm thick Au film [27].

This energy transfer of the electron to the lattice causes a rapid thermal expansion that results in photo-induced stresses in the material. The relaxation of this thermal expansion causes mechanical vibrations, the acoustic phonons, in the material [28] [29] [30]. Figure 6 shows a schematic of different events happening in ultrafast laser ultrasonics [31].

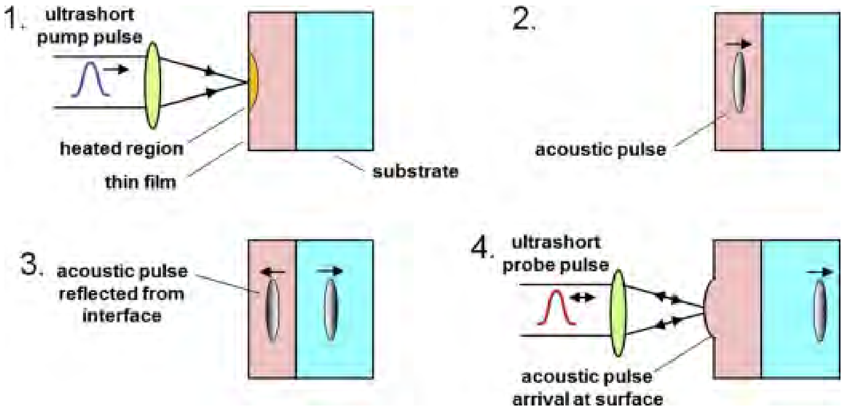

**Figure 6.** Series of events in picosecond laser ultrasonics on a sample with a thin metal film on a substrate [31].

One of the advantages of using an optical pump-probe technique, is the possibility for non-contact photoacoustic measurements. In addition to this, the spot size that determines the frequency range that is excited, can be tuned independent of the sample. This allows for a much broader spectrum of frequencies that can be excited on the sample. The acoustic wavelength excited by IDTs is determined by the geometry of the IDT and is therefore less tunable. Changing the desired excitation frequency would require a new sample with different parameters of the IDT [32]. The ability to adjust the excited frequency spectrum is a very useful property, that allows to perform measurements inside, outside and at the edge of the bandgap.

A notable phenomenon that could influence the acoustic waves is the difference in thermal expansion coefficients between the substrate and the coating. This mismatch can result in residual stresses in the coating that influence the velocity of the acoustic wave. The precise relation between the velocity of the acoustic wave and the residual stress in the coating is very complex and often the effect is very small [33] [31], therefore it will be neglected in this thesis.

## 2.3 Pump-Probe Laser Reflectometry

The generation and detection of acoustic waves can be achieved through the application of pump-probe lasers. The pump, a femtosecond pulse, excites the solid that results in the emission of a phonon caused by the mechanisms discussed in Section 2.2.2. A time delayed laser pulse, the probe, is used to detect the phonon present in the membrane. This detection is done by measuring the changes in transmission/reflection of the probe beam, that are caused by the phonon, with a photodiode. By gradually increasing the time delay between the pump and the probe laser, the dynamic behavior of the phonon can be measured and reconstructed [34].

At TU Delft, an Asynchronous Optical Sampling (ASOPS) pump-probe setup with Beam Distortion Detection (BDD) was developed by M. Robin et al. [10]. In ASOPS, the pump and probe laser are coupled together with a small difference in repetition rate given by $\Delta f$. Due to this small offset, and by gradually increasing this offset, the probe laser slowly scans the signal [35]. In addition, BDD is a non-contact method that allows for measuring acoustic waves. The thermal expansion of the sample caused by the laser excitation creates a curvature on the surface of the sample. The divergence of the probe laser that is reflected of this curved surface changes depending on the curvature. When passing through pinhole, the power that reaches the detector also changes depending on the curvature. This way the acoustic wave can be reconstructed. Figure 7a shows a visualization the ASOPS working principle. Figure 7b shows and a schematic of the BDD method.

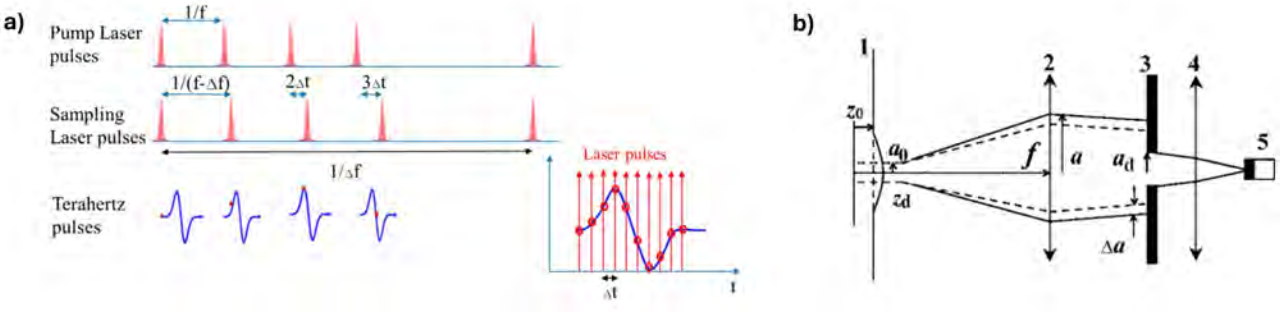

**Figure 7.** The two key concepts used in the pump-probe setup at TU Delft. **a)** Schematic of the ASOPS method that reconstructs the signal by sampling at an offset of $\Delta f$ to the pump laser. **b)** BDD concept where 1: Sample, 2: Objective, 3: Iris diaphragm, 4: Focusing lens, 5: Detector [35][36].

However, the setup introduced in the work of M. Robin et al. has been modified. The most significant changes are the absence of a birefringent crystal, the introduction of a balanced photodetector for better sensitivity and the possibility to add a mask to the path to the pump laser. The modified setup can be seen in Figure 8. This setup will be discussed in detail in Section 3.4.

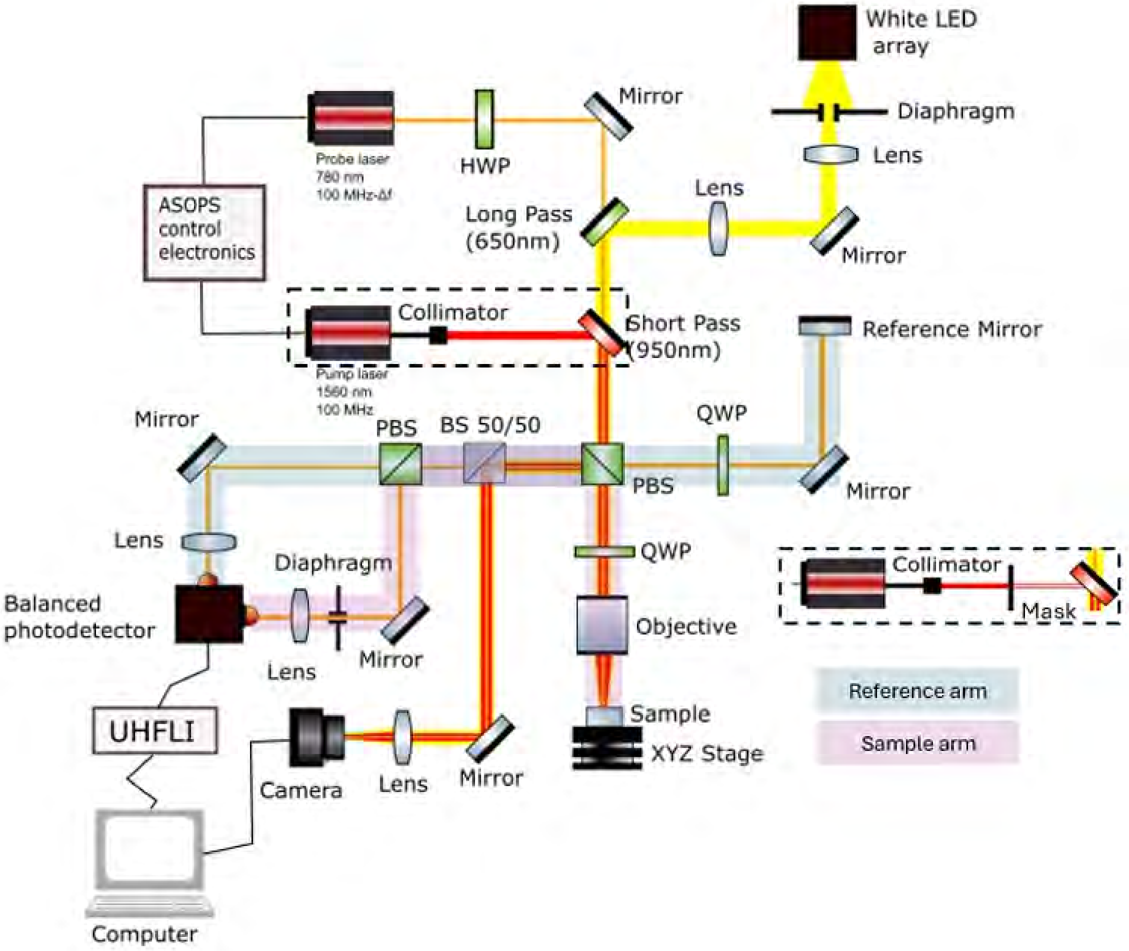

**Figure 8.** Schematic of the pump-probe laser setup at TU Delft (HWP: Half-Wave Plate, QWP: Quarter-Wave Plate, (P)BS: (Polarizing) Beam Splitter) [9].

To be able to generate waves that are within the band gap of the PnC, it is preferred that the frequency of the excited waves is tunable. In his Msc thesis, A. Soltész showed that by placing a mask consisting of two holes of diameter $d$ at distance $l$ from each other in front of the pump laser, an interference pattern occurs on the sample. The created mask can be seen in Figure 9a, the integration of the mask is shown in Figure 9b.

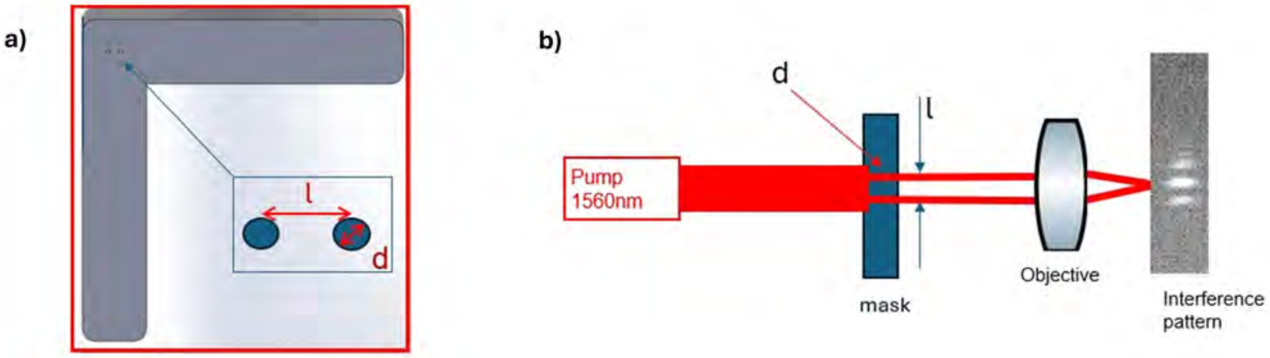

**Figure 9.** Proposed pump-laser mask by A. Soltész for tunability of the excited waves, where $d$ is the diameter of the holes and $l$ the distance between the holes. **a)** 3D model of the mask. **b)** Integration of the mask in the laser path [9].

By varying the distance $l$ and the diameter $d$, the spacing and thickness of the dark and bright fringes of the interference pattern can be changes. The different interference patterns will result in different frequencies of the excited waves [37]. The mask was tested with the probe laser, which is better detectable with a camera due to the fact that the wavelength is in the visible light range. An almost linear relation was found between the aperture distance and the fringe distance. However, testing the excitation frequencies for varying aperture distances did not give the desired results. Due to the small $d$ of the apertures, only a small amount of the laser power passes through the mask and reaches the sample. This resulted in a low signal-to-noise ratio, providing no hard evidence for the effectiveness of the mask [9].

## 2.4 State of the Art

This subsection will provide relevant studies that have been done to proof the possibility to guide and split acoustic waves. The latest advancements in the field will be discussed and gaps in the presented works will be addressed to form the framework of this thesis.

### 2.4.1 Phononic Beam Splitter Based on Self-Collimated SAWs [38]

The aim of this study was to numerically show self-collimated SAWs based on PnCs and splitting them using geometrical line defects in Pncs. The PnC used in this study is a cone-shape micropillar in a square lattice, placed on an isotropic substrate. The used lattice constant is $a = 1\mu m$, the other dimensions of the micropillars are $r = 0.25\mu m$, $h = 0.4\mu m$ and $\alpha = 82°$. The thickness of the piezoelectric substrate is $8a = 8\mu m$. The model is shown in Figure 10.

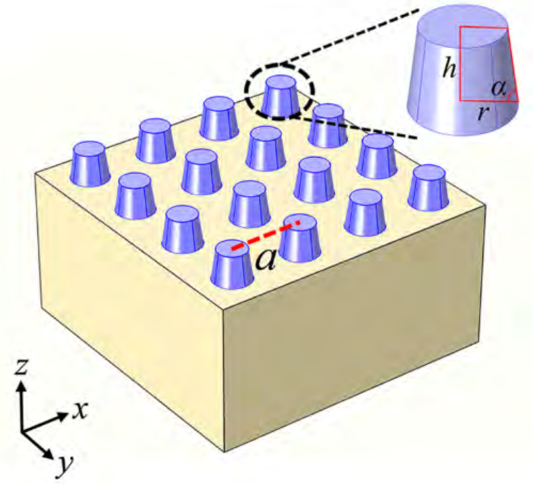

**Figure 10.** Model of cone-shaped micropillars in a square lattice on top of a piezoelectric substrate, with it's corresponding parameters.

After finding the wave frequency at which self-collimation is best, a beam splitter is proposed. This beam splitter is created by changing the radius of the micropillars along a line defect, see Figure 11a. The ratio of how much energy of the wave is deflected or transmitted, can be modified by changing the radius of the micropillars according to Figure 11b.

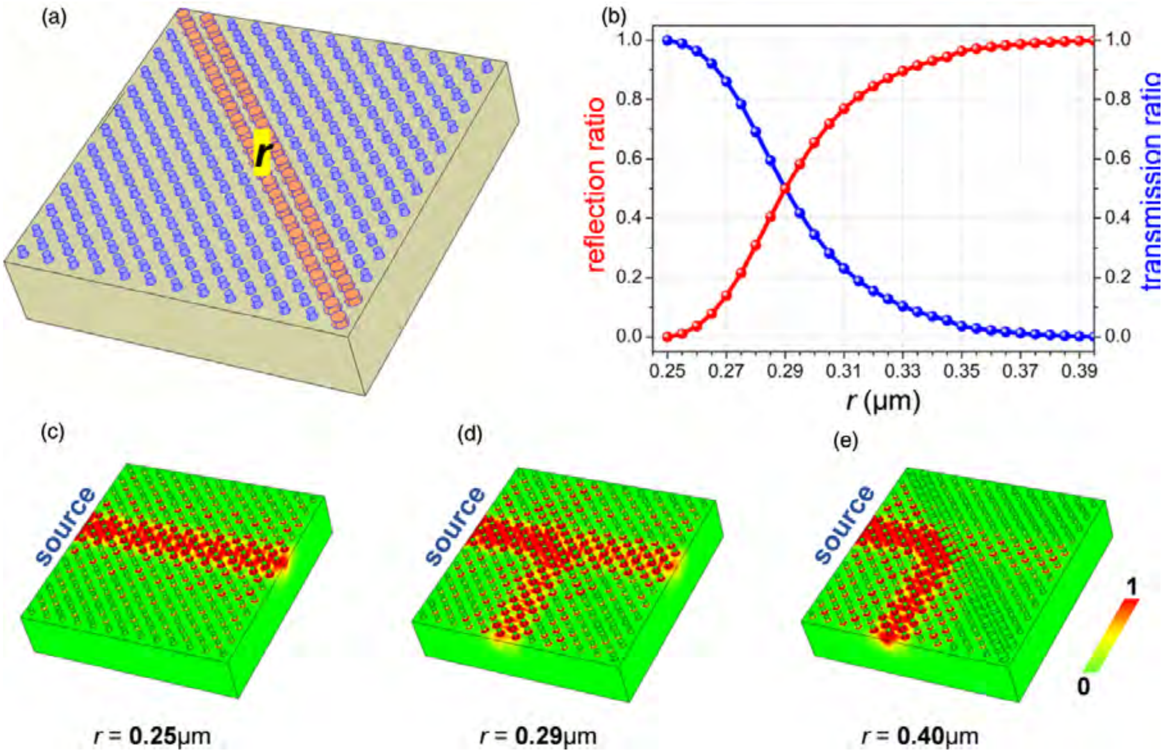

**Figure 11.** SAW transmission and deflection of micropillars with varying radii. **a)** Micropillar lattice with rows of changed radius in red. **b)** Deflection and transmission for various radii. **c)** Full transmission for r=0.25$\mu$m. **d)** Equal deflection an transmission for r=0.29$\mu$m. **e)** Nearly full deflection for r=0.40$\mu$m.

Figures 11c-e show the energy ratio of the splitting for different values of $r$. In the case of $r = 0.25\mu m$ the wave is fully transmitted, as the radii of micropillars in the square lattice and the line defect are equal. By slightly increasing the radii to $r = 0.29\mu m$, half of the wave is deflected and half of the wave is transmitted. Finally, increasing the radii to $r = 0.40\mu m$, the wave is almost fully deflected.

This study numerically proves that bending and guiding SAWs is possible by changing the parameters of PnCs in the line defect. By properly choosing the radius of the micropillars, the desired ratio of deflecting and transmitting the energy of the can be realized. Experimental validation of the obtained numerical results is not presented in this study.

### 2.4.2 Tightly Confined Guiding and Splitting of SAWs Using Line Defects in PnCs [39]

The waveguide used in this study consists of line defects in a lattice of nickel pillars, the PnCs, deposited on top of a lithium niobate substrate. To generate the SAWs propagating through the waveguide, interdigitated transducers (IDTs) are used. As discussed in Section 2.2.2, the IDTs are able to generate SAWs due to an alternating stress and strain field in the substrate. The schematic of the IDTs and the waveguide can be seen in Figure 12a. Figure 12b and 12c show the dimensions of the PnC pillars and a Scanning Electron Microscopy (SEM) close-up of the PnC pillars respectively.

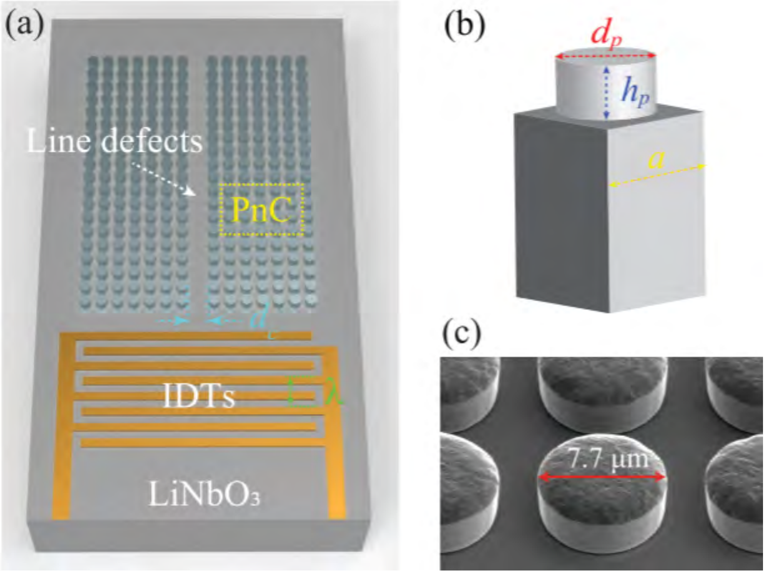

**Figure 12.** Sample setup to guide SAWs. **a)** Schematic of the waveguide and IDTs. **b)** Unit cell of PnC with it's parameters. **c)** Close-up of the nickel pillar PnCs.

By Finite Element Method (FEM) analysis, the mid band gap frequency of PnCs shown in Figure 12 was identified at 200 MHz with a upper limit around 215 MHz and lower limit of around 185 MHz. These results were verified by exciting 200 MHz SAWs and measuring the z-displacement before and after 41 rows of PnCs. The resulting out-of-plane displacement can be seen in Figure 13a and clearly shows that the propagation of the SAW is prohibited by the PnCs. Figure 13b show the out-plane-displacement plotted against the frequency.

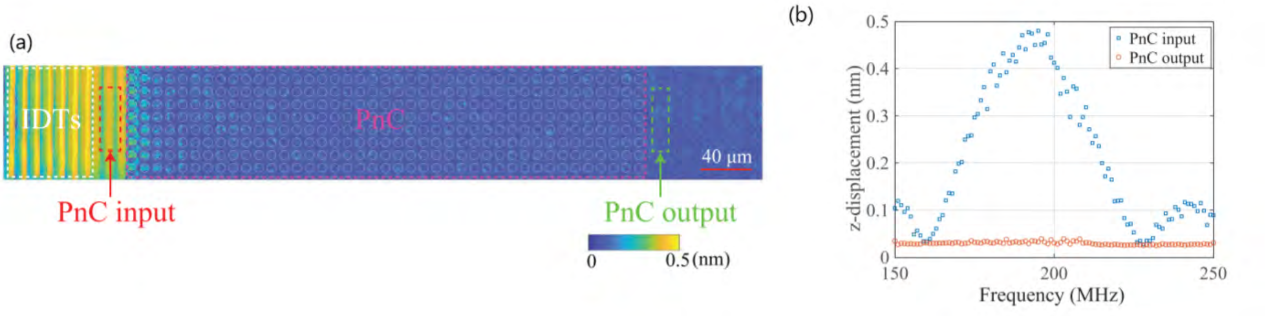

**Figure 13.** Experimental result of SAW attenuation. **a)** Z-displacement map of excited SAW. **b)** Z-displacement spectra at the input and output.

After confirming the band gap created by the PnCs, waveguides of different geometries are presented: a straight waveguide, a 90° waveguide and a SAW splitter. The results following from the 90° waveguide and the SAW splitter are the most interesting as they include straight guiding, bending and splitting of the SAW. The z-displacement map of the 90° waveguide and the SAW splitter are shown in Figure 14.

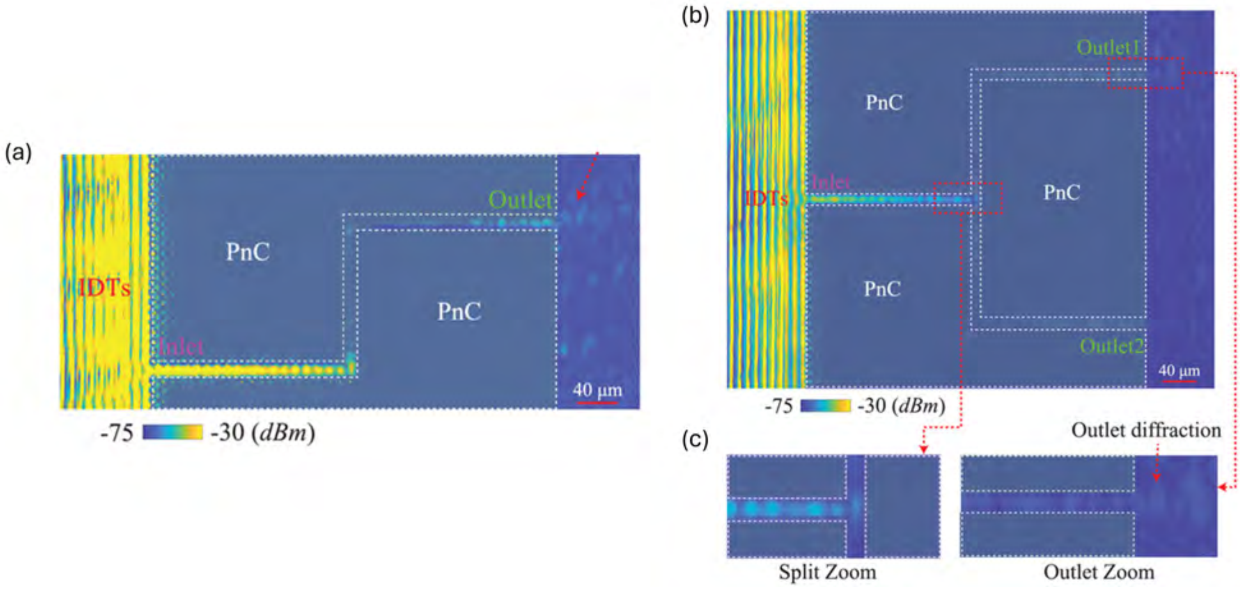

**Figure 14.** Experimental results of guiding and splitting SAWs. **a)** Z-displacement in S-shaped waveguide. **b)** Z-displacement in splitter. **c)** Zoom-in view of the Z-displacement at the splitting section and at the outlet.

The configurations shown above provide experimental data of successfully guiding and splitting SAWs. However the waveguides show relatively high attenuation of the SAW, especially at the split and in the corners. A possible cause for this strong attenuation is the backscattering of the SAWs when interacting with the PnCs. To minimize this effect, the geometry of the PnCs can be optimized such that the trade-off between confining the and attenuation the SAW is best. Another solution might be to change the lattice of PnCs, this could reduce the effects of backscattering and leaking at the corners and the split section.

### 2.4.3 Guiding and Splitting Lamb Waves in Coupled-Resonator Elastic Waveguides [40]

To reduce the energy loss to the substrate, PnC slabs are investigated more intensively. These PnC slabs have a small thickness compared to the length and width of the slab. Because of this, the free surfaces of the slab strongly confine Lamb waves. Multiple studies show the numerical results of strongly confining Lamb waves along line defects in waveguides. However this study provides experimental results of confining Lamb waves along coupled-resonator elastic waveguides (CREWs). The main motivation for using CREWs instead of PnCs, is the ability to simultaneously have high confinement of the wave while having a low group velocity transmission. Figure 15 shows the unit cell of CREWs used in this study.

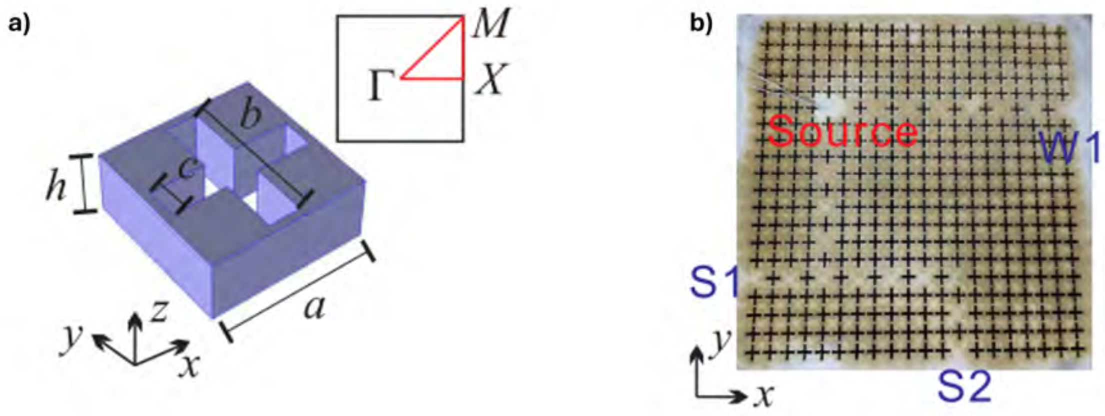

**Figure 15.** Materials used in this study. **a)** Unit cell of the coupled resonator. **b)** CREW with the source in labeled red. The outlet of the straight waveguide is label with W1, the outlets of the splitter are labeled by S1 and S2

With this waveguide, Lamb waves of three different frequencies inside the band gap were excited at the source (shown in Figure 15b). The results for these three different frequencies are quite similar, only the amplitude of the generated waves differs. For this reason, only the result for a 87.81 kHz Lamb wave is shown in Figure 16. The left image shows the result for the straight waveguide, while the right image shows the result for the wave splitter.

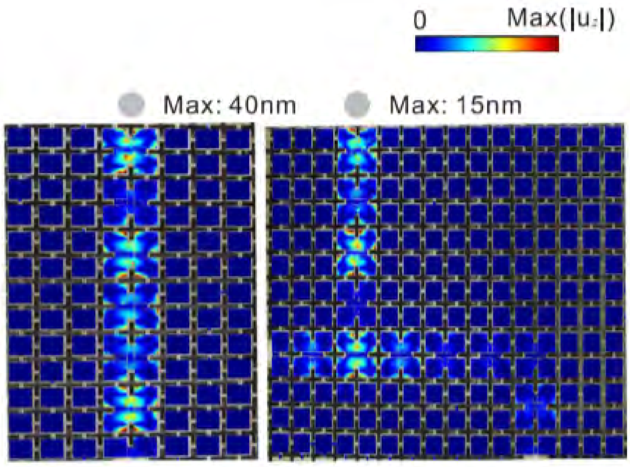

**Figure 16.** Experimental results of a 87.81 kHz Lamb wave in the CREWs waveguide, showing clear confinement to the waveguide.

The straight waveguide shows that the Lamb wave is strongly confined, with good transmission in the direction of propagation. The right image clearly shows the splitting of the Lamb wave to both sides of the splitter, with acceptable attenuation. In addition to this, bending of the wave by a 90° angle is also observed. These results are promising for more complex waveguides and waveguides with longer paths.

## 2.5 Theoretical Summary

In literature, there are various studies showing the possibility to guide, bend and split acoustic waves. The use of PnCs and CREWs both strong confinement of the acoustic waves within the waveguide. A strong attenuation of SAWs can be seen when encountering a 90° corner or a split. For Lamb waves, the attenuation at the same geometric interfaces was less. However this result was obtained with the use of CREWs, instead of PnCs. For Lamb waves in waveguides that consist of PnCs, the attenuation is unknown.

Excitation of the acoustic waves can be done through the use of IDTs or with a pump-probe laser setup. As the pump-probe laser setup offers a more broadband frequency range for excitation and the measurements are non-destructive, this method is preferred. The setup showed by A. Soltész that is available at TU Delft, will be used. The mask used to tune the excited waves will have to be tested and improved further to decrease the power loss of the pump laser.

# 3 Methods

This section presents the methods and materials used in this thesis. First the fabricated suspended membranes that are used in the measurements are discussed. Then the COMSOL models of the membranes and the wave propagation that will be used for simulations, are introduced. The laser setups used to conduct the experiments are explained after this. Finally, the Acousto-Optical Modulator that is implemented is shown.

## 3.1 Suspended Membranes

All measurements are performed on a sample containing five different configurations of waveguides. These waveguides are fabricated on a thick Si substrate, which is coated with a 200 nm layer of $Si_3N_4$ that is pre-tensioned at 1 GPa. A 20 nm gold film is deposited on top of the $Si_3N_4$ to enhance absorption of the laser. By etching away the underlying Si, the waveguides are left suspended. The five configurations of waveguides, shown in Figure 17, differ in PnC lattice and line defects to allow guiding, splitting and interference of acoustic waves.

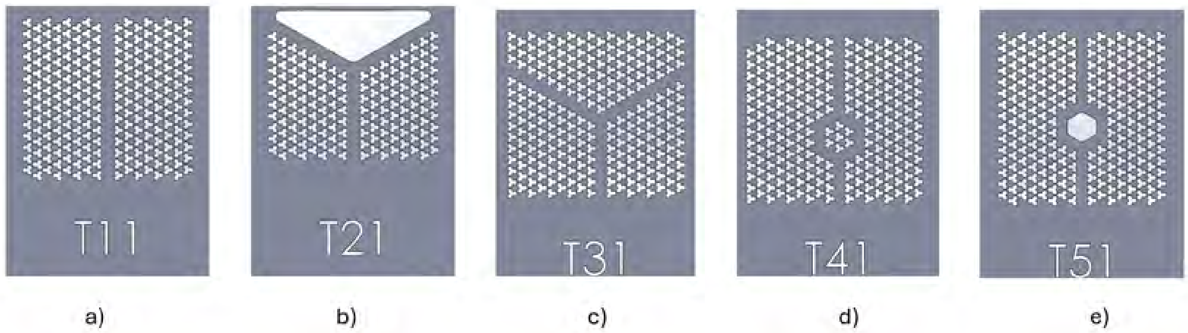

**Figure 17.** The five configurations of the fabricated suspended membranes. The lattice constant of these membranes is $a = 10\mu m$. **a)** Straight waveguide. **b)** Hard splitter. **c)** Soft splitter. **d)** Soft interferometer. **e)** Hard interferometer [9].

Three distinct paths are defined through the PnC lattice. Figure 17a shows a straight waveguide. Figures 17b and 17c both start as a straight waveguide, that splits into two similar branches, each angled at 60°. Figures 17d and 17e show an interferometer that splits the incoming wave and recombines it at the output. In Figures 17b and 17e, the boundary where the wave is split consist of one large air gap instead of a PnC lattice. This so called 'hard splitter' possibly results in different splitting behavior.

To allow for different phononic bandgaps in the waveguide, the fabricated chip contains multiple variations of each geometry. For each variation, a different lattice constant is used: $a = 25\mu m$, $15\mu m$, $10\mu m$, $6\mu m$, $4\mu m$, $2.5\mu m$ and $1.5\mu m$. For each lattice constant, there are five waveguides where the lattice constant is further varied by 1% to obtain a broad spectrum of phononic bandgaps.

To determine the frequency that will be confined in the waveguide after excitation, COMSOL simulations of an infinitely repeating and fully suspended unit cell of the PnC are done for each lattice constant [9]. These simulations resulted in the following theoretical bandgaps for each lattice constant:

- a = 25 $\mu$m: 90 MHz - 165 MHz
- a = 15 $\mu$m: 150 MHz - 265 MHz
- a = 10 $\mu$m: 250 MHz - 400 MHz
- a = 6 $\mu$m: 390 MHz - 660 MHz
- a = 4 $\mu$m: 530 MHz - 1.05 GHz
- a = 2.5 $\mu$m: 800 MHz - 1.6 GHz
- a = 1.5 $\mu$m: 1.5 GHz - 2.8 GHz

The fabricated sample will most likely exhibit manufacturing imperfections, which can alter the formation of a bandgap. In addition to this, the PnC lattice is finite with a fixed boundary (unlike the previous simulations of an infinitely periodic lattice). This change is also likely to influence the bandgap. Therefore, the values mentioned above serve as an indication and need to be verified further for individual membranes.

## 3.2 COMSOL Models of Suspended Waveguides

The bandgaps that were established for the different lattice constants, were found by doing COMSOL simulations of a fully suspended and infinitely repeating periodic lattice of PnCs [9]. However, the manufactured membranes are finite lattices of PnCs with line defects and fixed boundaries, which can alter the bandgap of the membrane. To validate the bandgap of the membranes, two of the membranes are replicated in COMSOL: Y15 with a lattice constant of $a = 24\mu m$ and T12 with a lattice constant of $a = 10\mu m$. The physics used in these simulations are either the Solid Mechanics or the Plate Mechanics. This depends on the need for an out-of-plane force in the simulation, since Solid Mechanics does not allow this in 2D. The boundary conditions for the membranes are 'Fixed' along the outer edge and 'Free' for the rest of the membrane. Figure 18 shows the COMSOL model of Y15 and and image of the actual manufactured waveguide, while Figure 19 shows the same for T12.

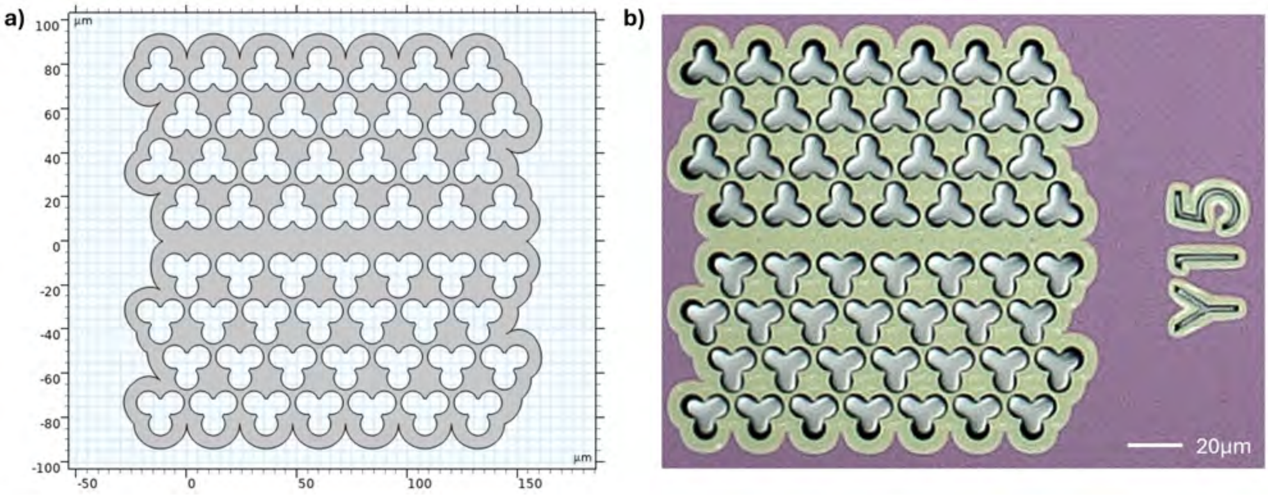

**Figure 18.** Waveguide Y15 with lattice constant $a = 24\mu m$. **a)** COMSOL model of Y15. **b)** Image of the manufactured Y15.

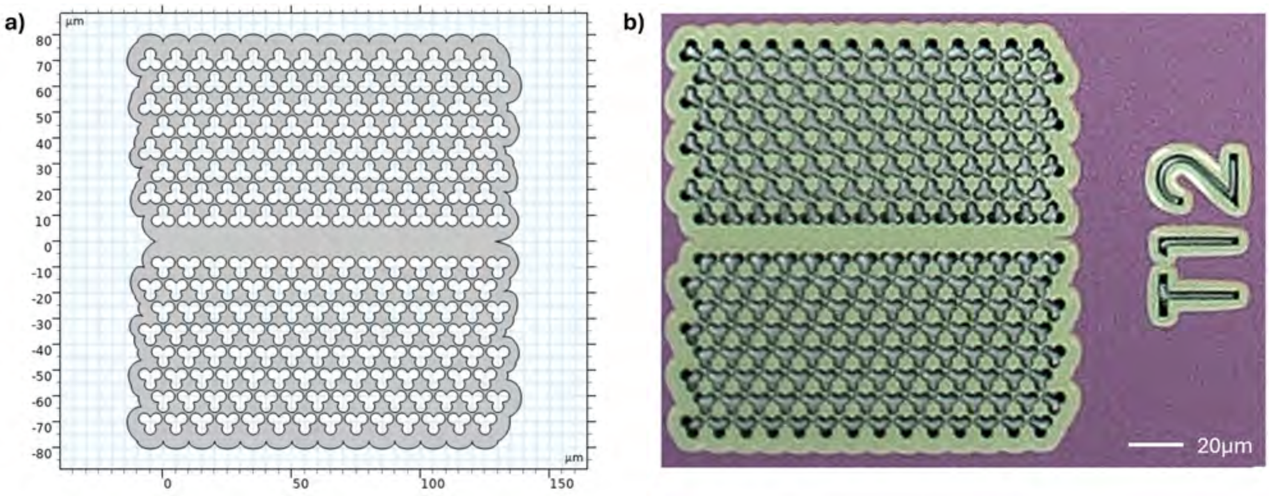

**Figure 19.** Waveguide T12 with lattice constant $a = 10\mu m$. **a)** COMSOL model of T12. **b)** Image of the manufactured T12.

The manufactured membranes consist of a 200 nm thick $Si_3N_4$ layer, coated with a 20 nm thick layer of gold. However, since the COMSOL simulations done in 2D, the membranes are modeled as 220 nm thick $Si_3N_4$ membranes, effectively approximating the combined thickness. In addition to this, the $Si_3N_4$ layer is pre-stressed to 1 GPa during fabrication. Upon suspension, the initial pre-stress redistributes throughout the membrane due to the geometry. This stress redistribution must first be computed and included into the model, since it can significantly affect the mechanical behavior of the membrane. After this redistribution is computed, additional simulations can be performed on the model.

One of these additional simulations is to compute the eigenmodes of a membrane around its predicted bandgap. Then, the density of the eigenmodes across the frequency spectrum can be plotted and individual mode shapes can be displayed to gain more insight in the exact shape of the bandgap.

In addition to this, the out-of-plane displacement across a specified frequency spectrum can be simulated, for different locations on the membrane. Using the plate mechanics in COMSOL, an out-of-plane point force can excite on the membrane (this acts as the pump laser). Adding a small circle to the geometry, COMSOL can use this circle to take a surface average of the displacement inside this circle (this acts as the probe laser). Varying the locations of both the point force and the surface averages, allows to plot the displacement across various locations of the membrane, induced by the point force.

## 3.3 COMSOL Simulation of Traveling Waves

To see if bulk wave that forms after laser excitation develops into a Lamb wave, a simplified simulation for wave propagation is done. For this, the Elastic Waves: Time Explicit physics in COMSOL is used. The model consist of a cross-section of a beam with the thickness of the suspended membranes (220 nm) and a length of 80 $\mu$m. The waveguides of the actual membranes have a length of $\sim$ 150 $\mu$m, but to save computational time this is almost halved. This will not directly influence the frequencies of the Lamb waves, since the bulk wave that forms the Lamb wave is only dependent on the thickness. The model can be seen in Figure 20.

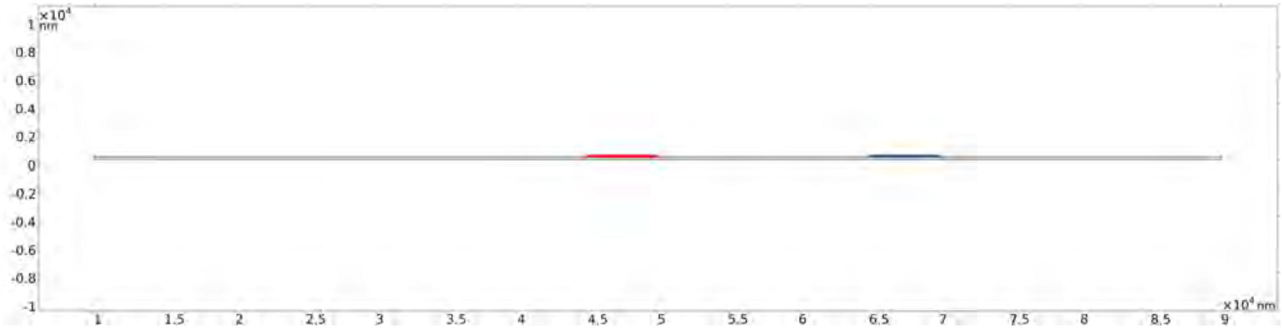

**Figure 20.** COMSOL model of the cross-section of a beam representing the waveguide. The red line segment represents the pump, while the blue line segment represents the probe.

In this model, the far left and far right side of the beam are given a fixed constraint. This mimics that the waveguide is fixed to the substrate on both ends. The red line segment on the left side of the model is given the excitation, while the blue line segment on the right is the probe boundary. Both line segments are 5 $\mu$m long, similar to the spot size of the pump and probe laser.

For the excitation of the bulk wave, an exponential decaying sinusoidal function is given to the line segment that represents the pump. This function is the following:

$$an1(t) = e^{-\frac{t}{\tau}} \cdot sin(2\pi f t) \tag{3}$$

where $\tau = 0.01$ ns is the decay of the signal and $f = 50$ GHz is the frequency of the input signal. Plotting this function gives the input signal shown in Figure 21.

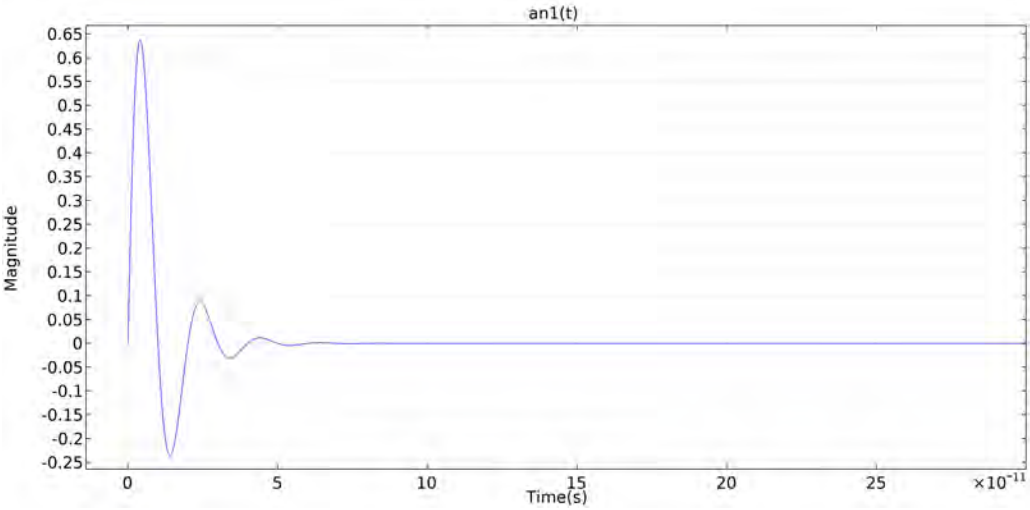

**Figure 21.** Input signal used to excite the bulk wave in the COMSOL simulation.

## 3.4 Pump-Probe Laser Setup

The pump-probe laser setup available at TU Delft is used for the measurements on the suspended membranes. In this setup, the pump laser only reaches the sample for excitation and the camera for alignment. The probe laser is split into a reference arm and a sample arm. The reference arm never reaches the sample and goes directly to the balanced photodetector. The sample arm reaches the other arm of the photodetector, after interacting with the sample. This way, the difference between the two arms determines the resulting signal. The white LED array is used to illuminate the sample so the pump and probe can be positioned at the desired locations. A schematic of the most recent state of the setup is shown in Figure 22. The pump and probe path will be discussed in more detail in Section 3.4.1 and Section 3.4.2 respectively.

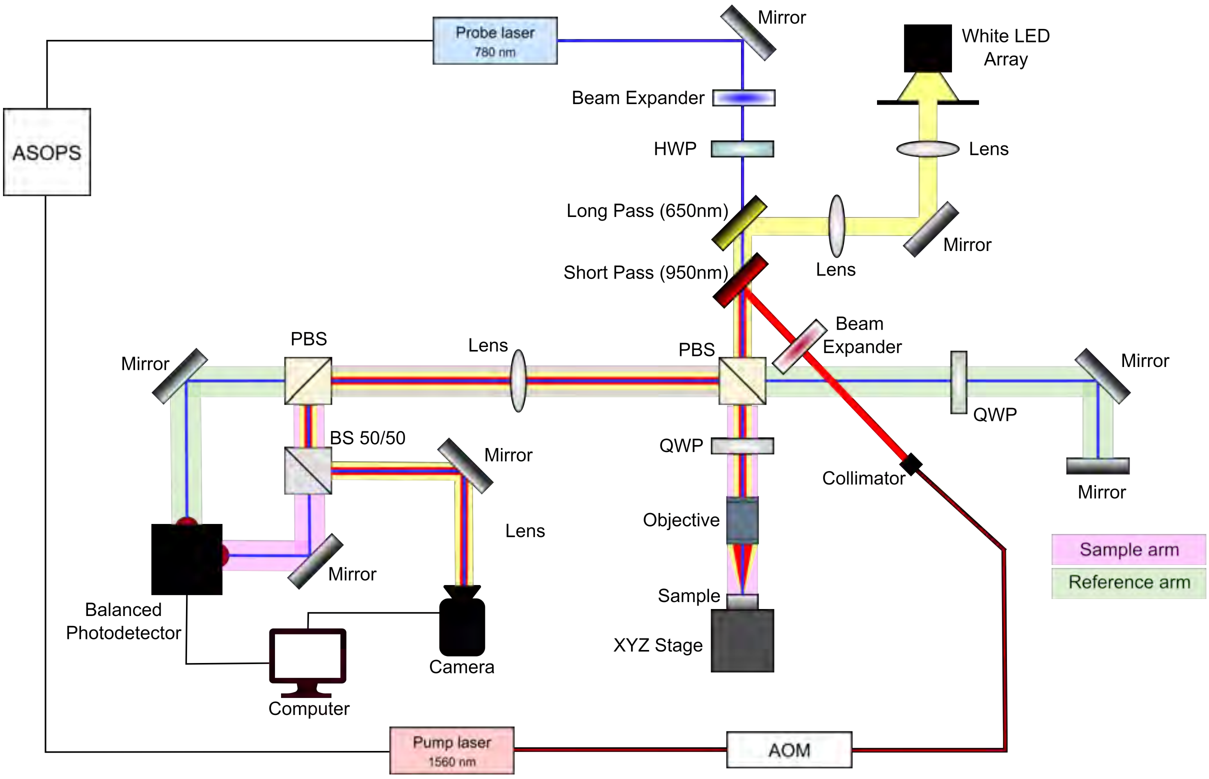

**Figure 22.** Schematic of the pump-probe setup at TU Delft. HWP: Half-Wave Plate, QWP: Quarter-Wave Plate, (P)BS: (Polarizing) Beam Splitter.

### 3.4.1 Pump Laser

The pump laser has a wavelength of 1560 nm with pulses of $\sim 100$ fs duration. The repetition rate of this laser is 100 MHz and has an average output power of approximately 100 mW.

After the pump laser leaves the fiber, it is first collimated by a collimator before entering the Beam Expander. The pump is then reflected at 45° to join the path of the probe laser. It then passes through the PBS, QWP and objective before it reaches the sample. The reflection is redirected by the PBS and enters the camera after a series of lenses, (P)BS's and mirrors.

### 3.4.2 Probe Laser

The wavelength of the probe laser is 780 nm with the same pulse duration of $\sim 100$ fs. The repetition rate of the probe is 10 kHz lower that the repetition rate of the pump. This offset is needed to slowly scan through the signal initiated by the pump laser and is managed by the ASOPS. The average power is around 5 mW.

Right after the probe laser leaves the laser box, it is reflected 90°. It then passes through a Beam Expander and a HWP, that determines the polarization of the light. The white light and pump laser are added to the path by a Long-Pass and Short-Pass dichroic mirror respectively. At the PBS, the probe is split into a reference arm and a sample arm. The ratio of this splitting can be changed by the HWP, that determines the polarization. This reference arm is deflected by 90°, while the sample arm passes through the PBS and reaches the sample. Both arms are then each directed to the Balanced Photodetector and camera by a series of lenses, (P)BS's and mirrors. The QWPs are used to split the input path from the output path.

## 3.5 Experimental Method

The main objective of the measurements is to distinguish the traveling wave from the modes of the membrane itself and then evaluate the behavior of the wave in different parts of the membrane. To achieve this, a systematic approach is needed for the measurements.

The probe is placed inside of the waveguide for these measurements and remains in this location throughout all the measurements. This is done to ensure that the membrane modes remain constant in the result of each measurement and only the behavior of the traveling wave changes. The exact location of the probe is shown in Section 4.9, where the individual measurements are shown.

The pump laser is placed at different locations inside the waveguide and is also placed in the PnC lattice. This way, the evolution of the wave can be seen for various distances. In addition to this, the wave should be heavily attenuated when the excitation is done in the PnC lattice with a bandgap that includes the frequency of the traveling wave. When this traveling wave is outside the bandgap, the magnitude should roughly be equal to the measurement inside the waveguide at an equal distance. The exact locations of the pump are also shown in Section 4.9.

## 3.6 Laser Interferometry Setup

The extracted resonance frequencies of the membranes give insight in the behavior of the membranes and can also be compared to simulations of the same membranes. This indicates how well the simulations match the experiments. To extract the resonance frequencies, a laser interferometry setup is available at TU Delft.

In this setup, a power modulated blue diode laser, with $\lambda = 404$ nm, actuates the membrane via the photothermal effect. The red He-Ne laser, with $\lambda = 632$ nm, is used to detect the motion of the membrane, since its reflected laser power depends on the position of the membrane. The VNA (Vector Network Analyzer) analyzes the reflected laser power of the red laser that is collected in the photodiode and transforms it to an amplitude in the frequency domain. This VNA also does the power-modulation of the blue laser [41]. A schematic of this setup is shown in Figure 23.

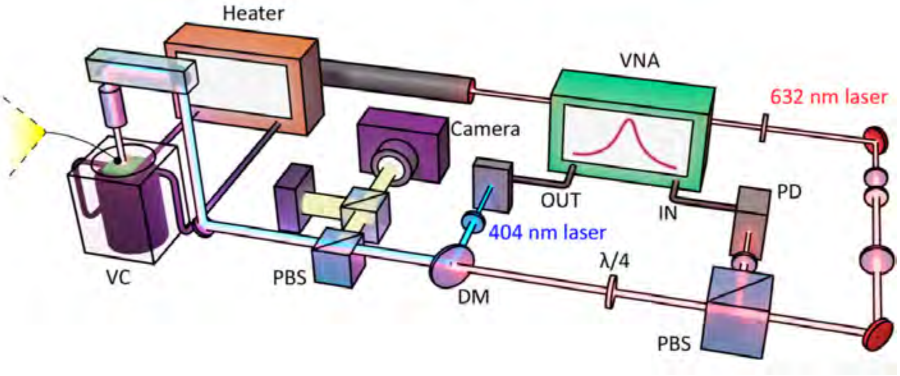

**Figure 23.** Laser interferometry setup available at TU Delft that is used to extract the resonance frequencies of the suspended membranes [41]. VNA: Vector Network Analyzer, PBS: Polarized Beam Splitter, PD: Photodiode, DM: Dirac Mirror, VC: Vacuum Chamber.

For the measurements on the suspended waveguide membranes, the vacuum chamber is not used. The sample is to large to fit into this vacuum chamber and was therefore mounted to the vibration-isolation table. Measurements without vacuum still reveal the most prominent resonances, only with a lower Q-factor.

### 3.7 Acousto-Optic Modulator

The frequency resolution of the FFTs is determined by the duration of the time-domain signal. This time-domain signal is directly linked to the repetition rate of the pump laser. Since the repetition rate of the pump laser is 100 MHz, a new pump pulse excites the sample every 10 ns. This limits the frequency resolution to a 100 MHz step-size.

To increase this resolution, the time between two consecutive pulses has to be increased (i.e. the repetition rate has to be decrease). To achieve this, a fiber-coupled AOM (Acousto-Optic Modulator) is added to the pump-probe setup. When there is no signal on the AOM, the lens at the input (left) side redirects the light such that it does not enter the output fiber. When a signal is put on the AOM, a sound wave propagates through the AOM cell that induces periodic variations in the refractive index of cell. The passing light experiences diffraction due to this varying refractive index. Controlling this diffraction angle allows light to enter the output fiber [42]. This way a selection of pulses can be transmitted to the sample. This is shown in Figure 24.

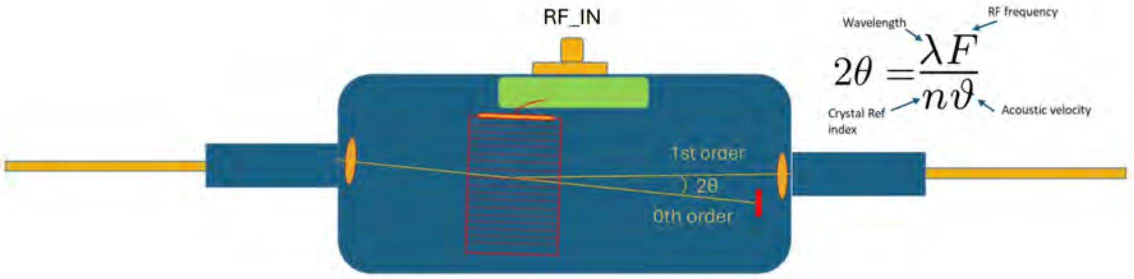

**Figure 24.** Working principle of the fiber-coupled AOM from AeroDiode. The angle between the 0th and 1st order is determined by: $2\theta = \frac{\lambda F}{n\vartheta}$ , for the indicated parameters [42].

In the ideal case, a pulse function is used as the signal that is put on the AOM. By tuning the parameters of this pulse function, one pump laser pulse can be transmitted and then a desired number of laser pulses is blocked. At the required timescales, the equipment used (MOKU:PRO) only gave clear experimental data when using a sine wave as input. Placing the peak of the sine at the first laser pulse and the bottom of the sine at the second laser pulse, allows to increase the time signal to 20 ns. This increases the FFT resolution to 50 MHz. Using a 10 ns pulsed input, electrical noise (crosstalk) with a larger amplitude than the acoustic signal, was seen in the data. In Figure 25, the used AOM with the corresponding driver can be seen.

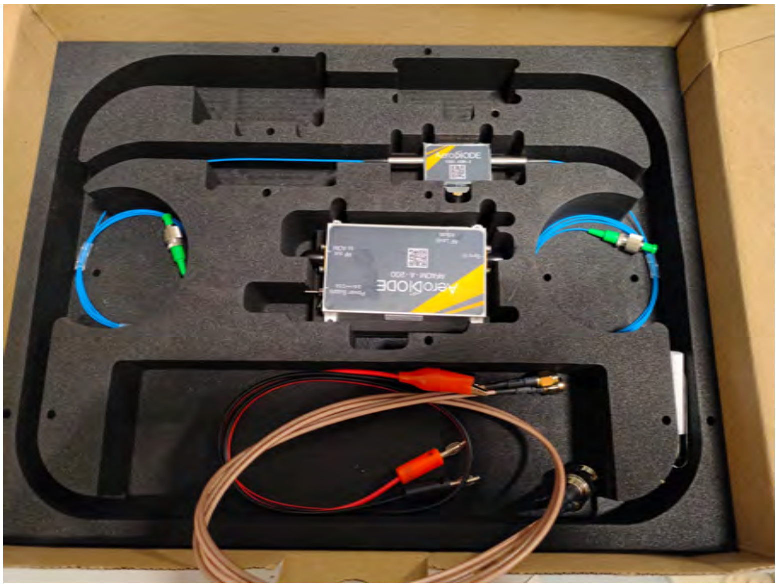

**Figure 25.** The AOM (top) with driver (bottom) of AeroDiode that is used in the measurements.

# 4 Results

The results obtained during this project, will be discussed in this section. First, the bandgap of two membranes are confirmed using COMSOL simulations. The spectrum of eigenfrequencies of two membranes, measured with the interferometer, will be compared to COMSOL simulations of the same membranes. After this, a simulated point displacement will be compared with photoacoustic measurements done on the membrane. Then measurements on the substrate are briefly discussed. Finally laser-induced damages done to the membrane are discussed.

## 4.1 Bandgap Simulation of Membrane Y15

After suspension, a stress redistribution of the 1 GPa pre-tensioned $Si_3N_4$ layer will occur. To better understand this redistribution, the simulation discussed in Section 3.2 is conducted. The result of this stress redistribution in membrane Y15, which has a lattice constant of $a = 24\mu m$, is shown in Figure 26. Within the waveguide, the tensile stress varies from approximately 0.5 GPa at location 1 to 0.95 GPa at location 2, due to the geometry of the PnCs. Inside the surrounding PnC lattice the stress ranges from around 0.2 GPa on the 'islands' between the PnCs (location 3) to significantly higher stresses of around 1.6 GPa on the narrow 'bridges' (location 4). Additionally, stress concentrations with peak values of up to 3.5 GPa can be seen at the sharp corners around the outer edge of the membrane (location 5). However, in the fabricated membranes, these type of corners are typically less sharp due to smoothing effects in the lithography and etching processes. This likely results in lower stress peaks in the fabricated membranes.

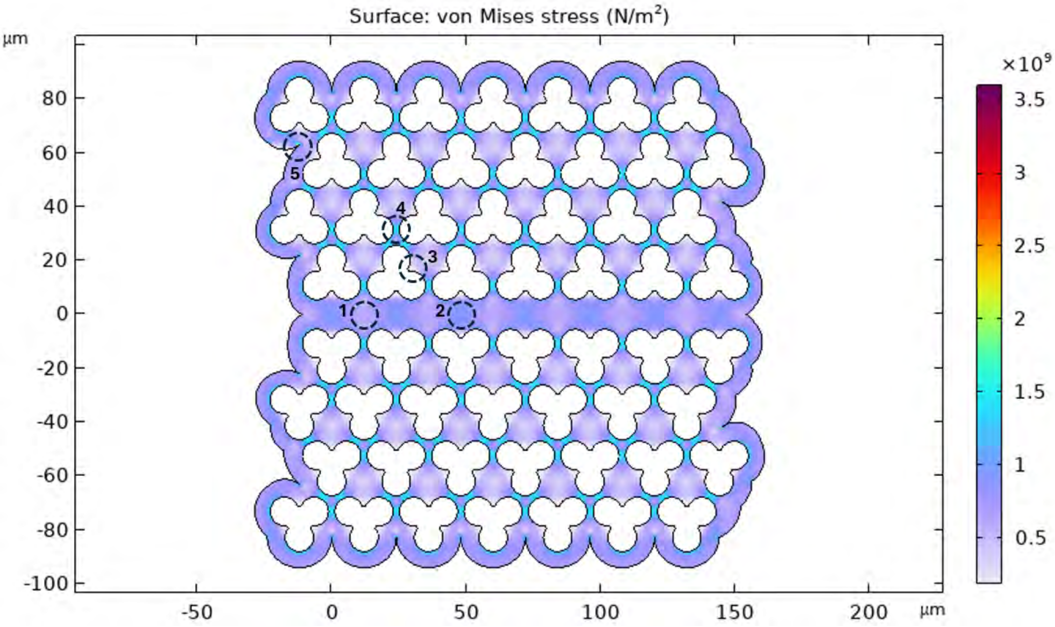

**Figure 26.** Stress redistribution in Y15, due to the 1 GPa pre-tensioned $Si_3N_4$ layer. Locations 1 and 2 indicate the highest and lowest stress inside the waveguide respectively. Locations 3 and 4 indicate the same, but inside the PnC lattice. Location 5 indicates the peak stress value of the whole membrane.

By computing the first 250 eigenmodes of membrane Y15, the corresponding eigenfrequencies are obtained and plotted to create the spectrum shown in Figure 27. These eigenmodes are calculated using the redistributed stress in the membrane, ensuring that the altered internal stresses are accounted for in the model behavior. The resulting graph shows the density of eigenmodes across the frequency domain and reveals well-defined regions where hardly any modes are present. These low-density regions, highlighted in gray, resemble the phononic bandgaps of the membrane. For membrane Y15, three well-defined bandgaps are seen in the frequency rangens of 90 MHz - 125 MHz, 130 MHz - 175 MHz and 185 MHz - 190 MHz.

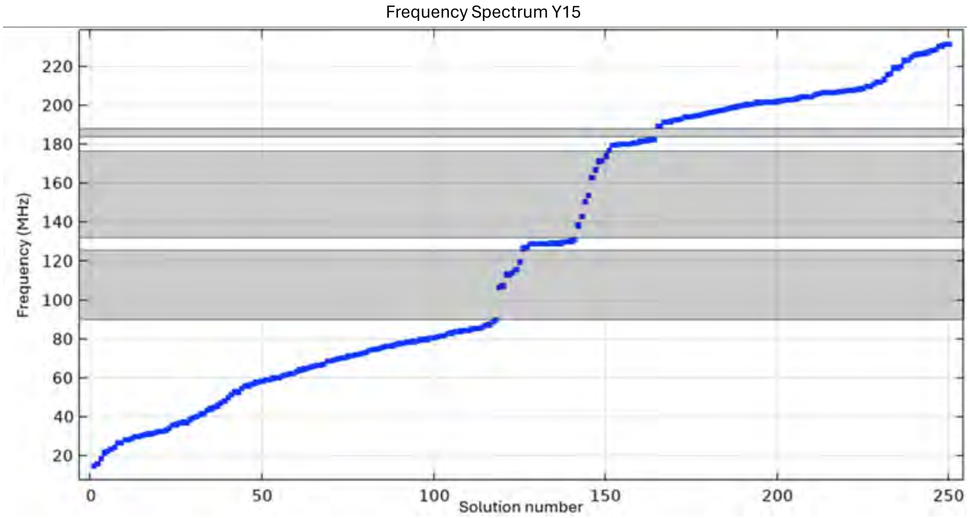

**Figure 27.** The first 250 eigenmodes of Y15 plotted with the corresponding frequency. Grey areas represent the possible phononic bandgap.

To further investigate the nature of the modes in the low-density regions, the out-of-plane surface deformation can be plotted for each individual mode. This reveals that the displacement of these modes is primarily localized within the waveguide or along the edge of the PnC lattice. For these modes, minimal to no deformation is observed in the bulk PnC lattice, indicating that these modes do not propagate through the periodic lattice. This means that the bandgap of the PnC remains intact and is not disrupted or split by these modes. Figure 28 shows two representative examples: in Figure 28a the mode concentrated along the edge of the membrane is depicted, while Figure 28b shows the mode confined to the waveguide.

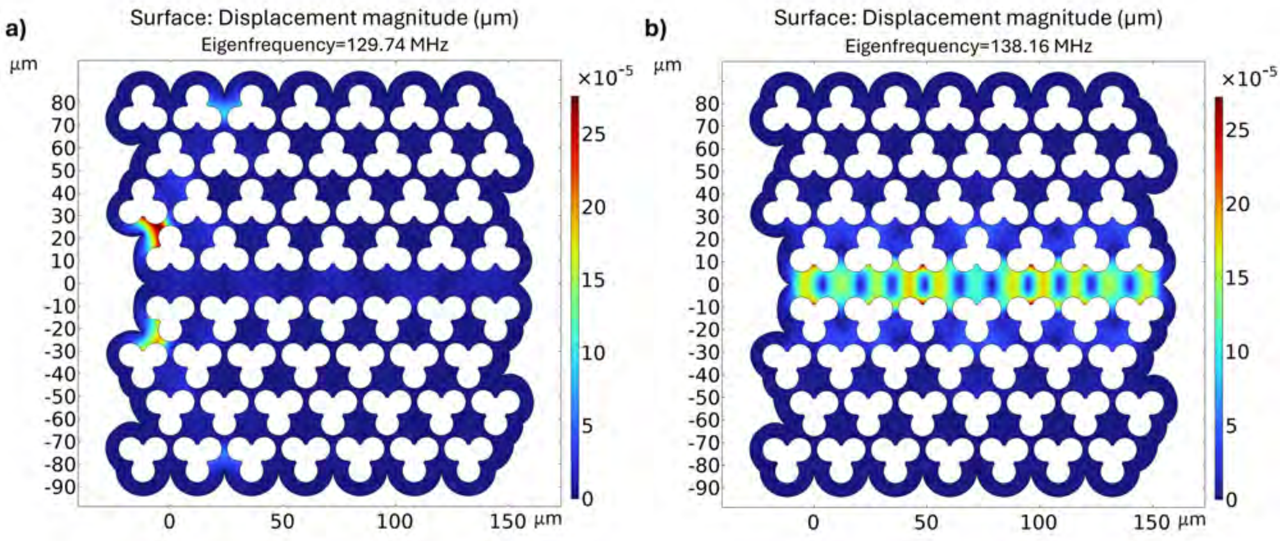

**Figure 28.** Two eigenmodes of Y15 within the bandgap. **a)** Mode localized along the edge of the membrane at 129.74 MHz. **b)** Mode localized inside the waveguide of the membrane at 138.16 MHz.

## 4.2 Bandgap Simulation of Membrane T12

An equivalent simulation of the stress redistribution in membrane T12, which has a smaller lattice constant of $a = 10\mu m$, is shown in Figure 29. The stresses within the waveguide of T12 are comparable to those seen in membrane Y15, ranging from 0.5 GPa at location 1 to 0.85 GPa at location 2. Inside the surrounding PnC lattice, the stress distribution is nearly similar to Y15. The lowest stress is again found on the 'island' (location 3), where it drops to around 0.2 GPa. The narrow 'bridges' again show higher stresses of around 1.7 GPa (location 4).

The peak stress at the sharp corners along the outline of membrane T12 (location 5) is notably lower than in Y15, reaching approximately 2.0 GPa. The maximum stress found in T12 is located at location 6, where the stress is around 2.5 GPa. This change in stress concentrations is likely due to the smaller lattice constant, resulting in a finer PnC lattice.

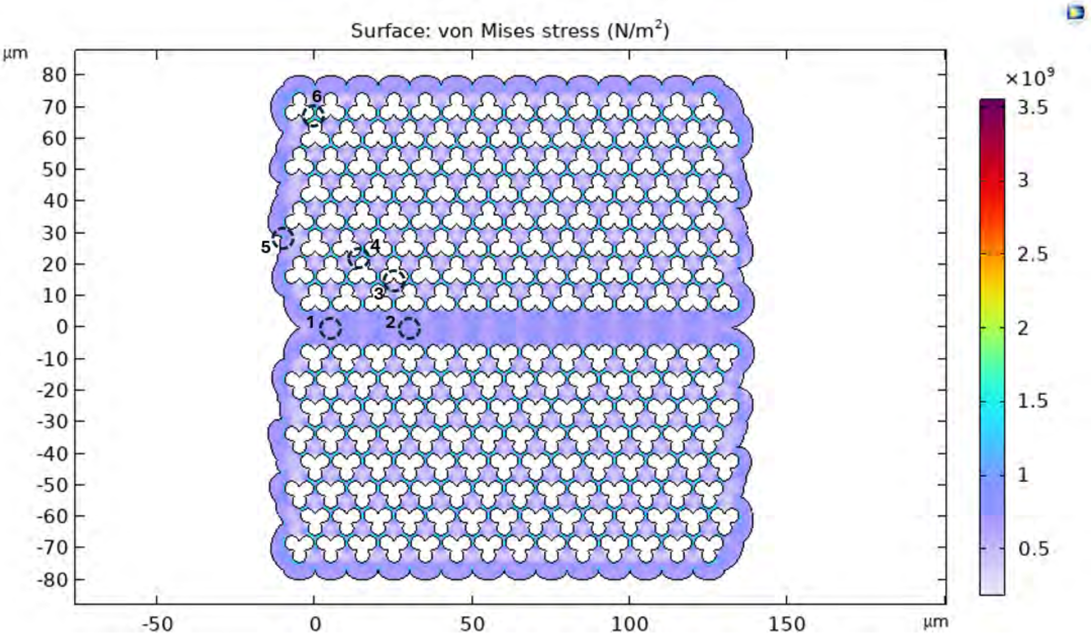

**Figure 29.** Stress redistribution in T12, due to the 1 GPa pre-tensioned $Si_3N_4$. Locations 1 and 2 indicate the highest and lowest stress inside the waveguide respectively. Locations 3 and for indicate the same, but inside the PnC lattice. Location 5 indicates the stress at a sharp corner, while location 6 now indicates the peak stress value of the whole membrane.

For membrane T12, the 400 eigenmodes closest to 350 MHz (center frequency of the bandgap predicted for an infinite periodic lattice with lattice constant $a = 10\mu m$ [9]) are plotted with their corresponding eigenfrequency, again with the stress redistribution accounted for. The resulting spectrum can be seen in Figure 30. Similar to membrane Y15, the distribution of eigenmodes shows well-defined ranges of frequencies in which fewer modes are present. These lower-density regions, the bandgaps, are highlighted in gray. For T12 the two bandgaps range from 210 MHz - 290 MHz and 320 MHz - 380 MHz.

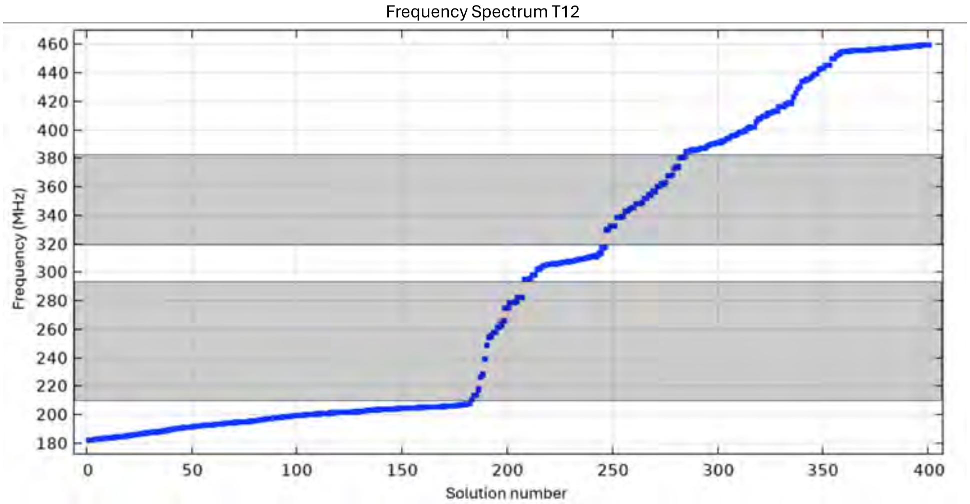

**Figure 30.** The 400 eigenmodes of T12 closest to 350 MHz, plotted with the corresponding frequency. Grey areas represent the possible phononic bandgap.

Again plotting the deformation of the surface of the membrane for each individual mode that is either within the bandgap or splitting the bandgap, reveals that these modes are once more localized to the outer edges of the membrane or inside the waveguide. Inside the bulk lattice of the PnC, little to no deformation is observed. Figure 31 displays two examples of these mode, where Figure 31a shows the mode along the edge of the membrane and Figure 31b the mode inside the waveguide.

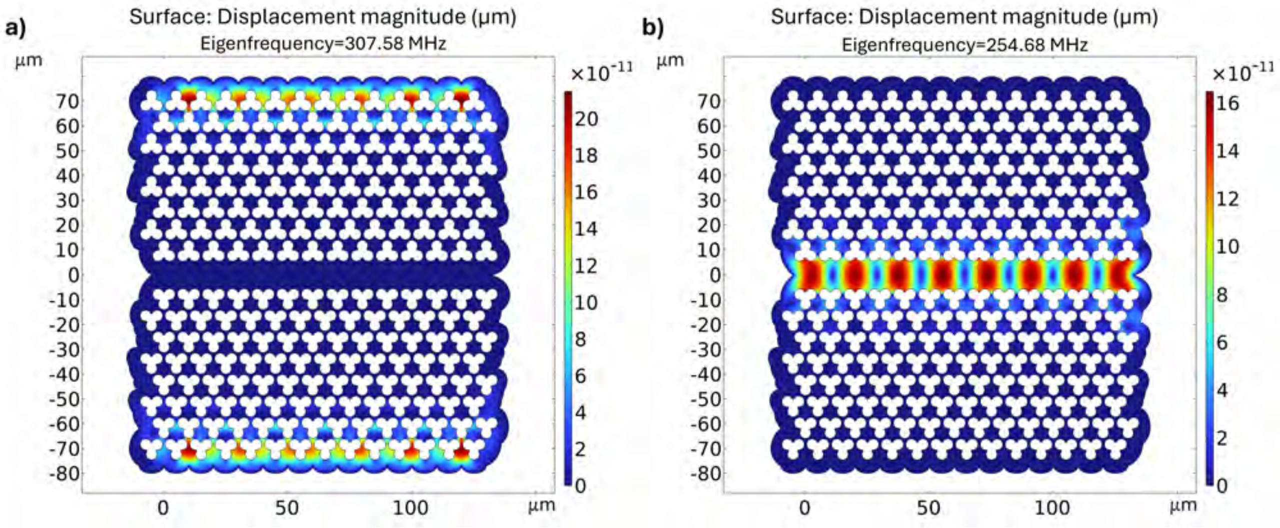

**Figure 31.** Two eigenmodes of T12 within the bandgap. **a)** Mode localized along the edge of the membrane at 307.58 MHz. **b)** Mode localized inside the waveguide of the membrane at 254.68 MHz.

## 4.3 Eigenmodes of Y15

The laser setup discussed in Section 3.6 is used to extract the resonance frequencies of membrane Y15. The overlapping red an blue laser placed inside the waveguide at the middle PnC. A frequency sweep is then performed from 5 MHz - 300 MHz. The result of this sweep and the location of the lasers can be seen in Figure 32. The most prominent resonances are indicated with the black arrows and the corresponding frequency.

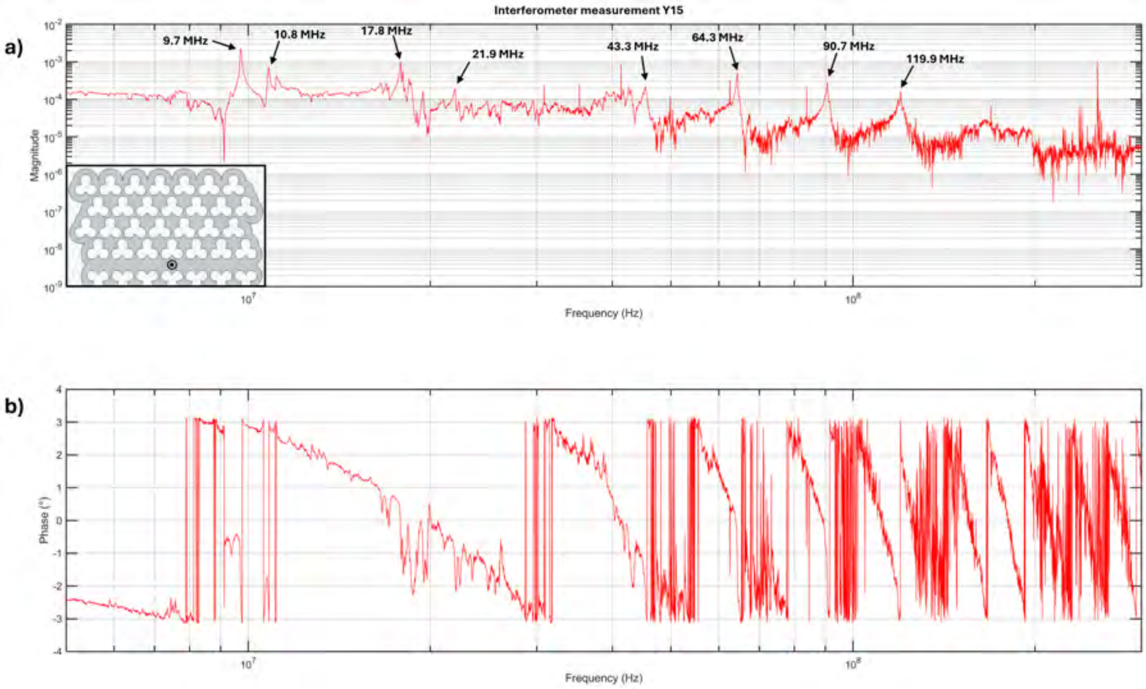

**Figure 32.** Interferometer results on Y15. **a)** Displacement magnitude of the point shown on membrane Y15. **b)** Phase plot corresponding to the measurement.

After this measurement, a simulation is done on the same membrane. A point excitation and a surface average displacement are placed at the same locations where the lasers were placed. Plotting the surface average displacement in the same frequency range as the measurement and overlaying it with the obtained results, gives Figure 33.

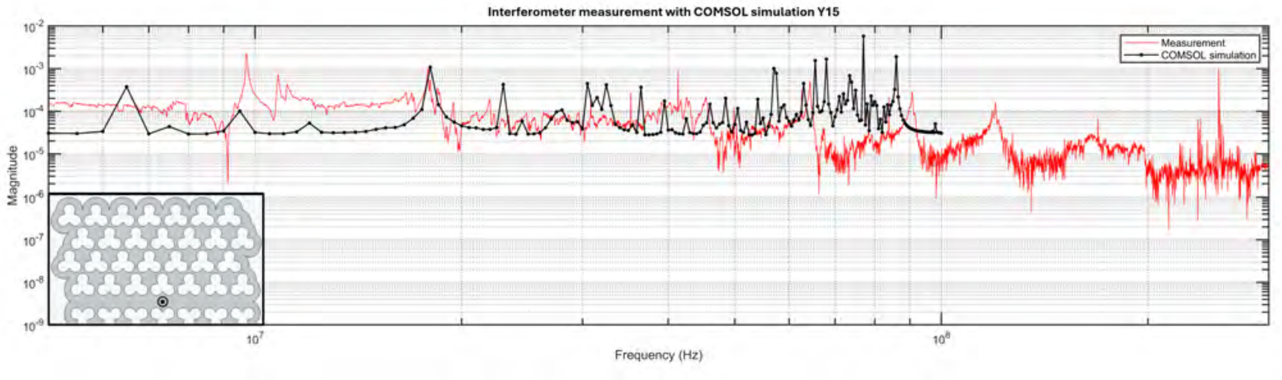

**Figure 33.** Displacement magnitude of the point shown on membrane Y15 in red, with the corresponding simulation in black.

In the graph of Figure 33, only a few modes of the simulation correspond to the measurement. The modes at 9.7 MHz, 17.8 MHz, 43.3 MHz are nearly identical in both the measurement and simulation. The mode at 90.7 MHz of the measurement is also visible in the simulation, but it is shifted by approximately 5 MHz.

There are multiple factors that might explain these differences. First of all, the results of the simulation are obtained with the assumption that the membrane is in vacuum. In the experiments, the air resistance can suppress modes due to damping, or shift them to a lower frequency due to the added mass of air.

The second factor, is the absence of the gold layer. This gold layer increases the thickness, mass and stiffness of the membrane, resulting in different resonances. The gold might also absorb the energy of the laser differently, which could alter the resonances. Finally, the thin gold layer can have its own resonances that will not show in the simulation.

The last factor is a result of an error in the manufacturing of the membrane. The process of etching away the Si substrate to create the suspension, was not done for the right amount of time. Due to this, the membranes with bigger PnCs are not fully suspended. The middle of the waveguide is still connected to the substrate. These 'pillars' can significantly influence the resonance frequencies. An example of such pillars can be seen in Figure 34 that is obtained by Scanning Electron Microscopy (SEM).

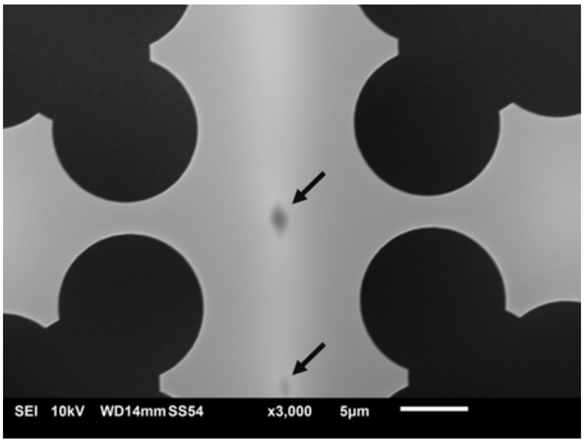

**Figure 34.** SEM image of pillars beneath the waveguide (indicated by the two black arrows) that prevent full suspension of the membranes.

## 4.4 Eigenmodes of T12

For membrane T12, again a frequency sweep is done from 5 MHz - 300 MHz. The red and blue laser are again overlapping and placed within the waveguide. The result of this experiment is shown in Figure 35. The black arrows indicate the most prominent resonances of the membrane.

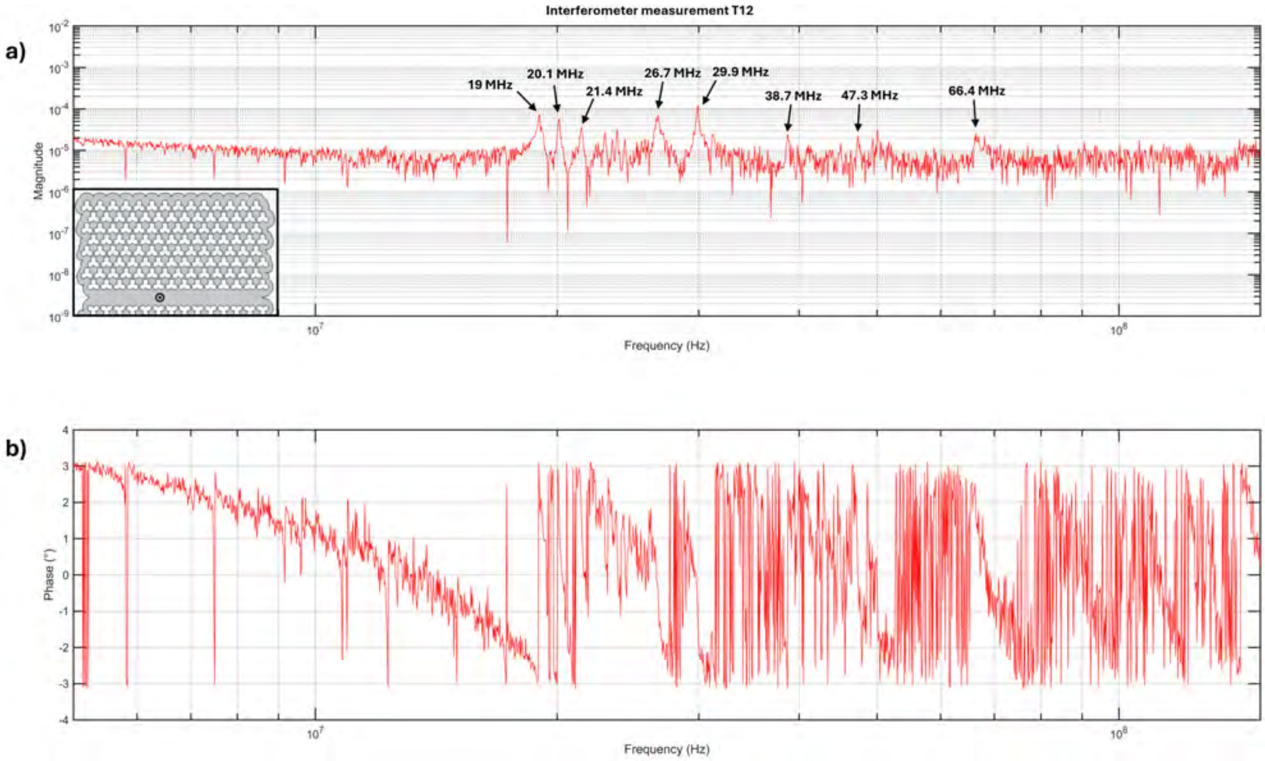

**Figure 35.** Interferometer results on T12. **a)** Displacement magnitude of the point shown on membrane T12. **b)** Phase plot corresponding to the measurement.

Again, a simulation is done for this membrane. The point excitation and surface average displacement are positioned similar to the measurement. This simulation is then plotted over the measurement. Figure 36 shows this.

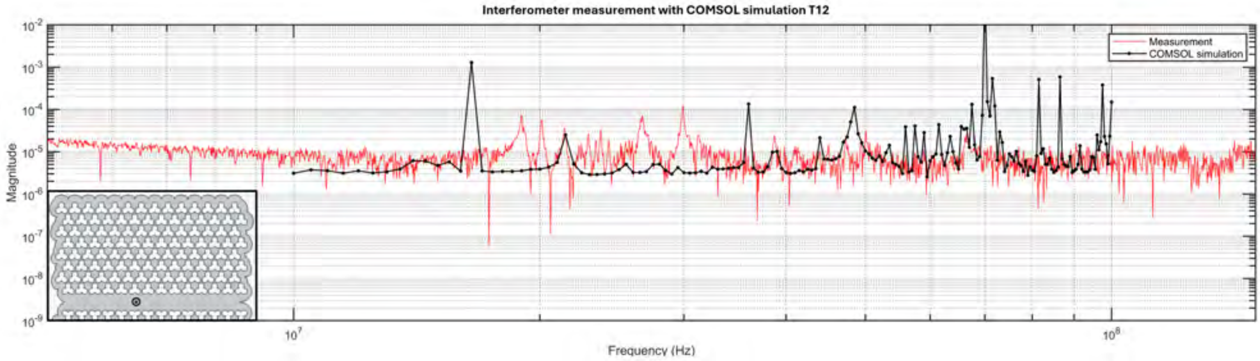

**Figure 36.** Displacement magnitude of the point shown on membrane T12 in red, with the corresponding simulation in black.

In this membrane, the modes from the simulation align better with the measurement than for membrane Y15. This is likely because membrane T12 is fully suspended, without under-etched pillars. However, there are still mismatched between the simulation and measurement. These mismatched can still be attributed to absence of vacuum and the missing gold layer.

## 4.5 Surface Displacement Simulation of Y15

In Figure 37, the result of overlapping the point force excitation and surface average displacement on an island inside the bulk PnC lattice of Y15 ($a = 24\mu m$) can be seen. This simulation is done for a frequency range of 100 MHz - 10 GHz and a step-size of 100 MHz (equivalent to the experiments).

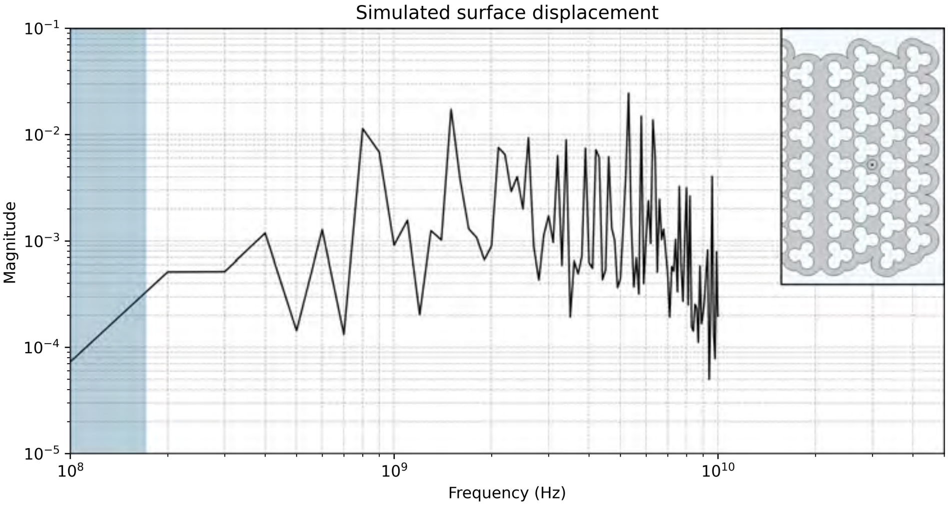

**Figure 37.** Simulated displacement of an island in the bulk PnC lattice of Y15 (100 MHz step-size). Blue area represents the possible phononic bandgap.

The PnC of membrane Y15 are expected to have a bandgap in the 90 MHz - 165 MHz range [9]. In the graph above, it is clear that the magnitude at 100 MHz (blue area) is a factor 10 less than the magnitude at 200 MHz. Since the graph starts at 100 MHz and has a step-size of 100 MHz, it is not evident if this drop at 100 MHz is an artifact and if the magnitude increases before the 200 MHz. In addition to this, the bandgap might extend into the region $< 100$ MHz. To confirm the bandgap of Y15, a new simulation with a decreased step-size of 1 MHz and a frequency range of 10 MHz - 1 GHz is done. The results of this simulation are shown in Figure 38.

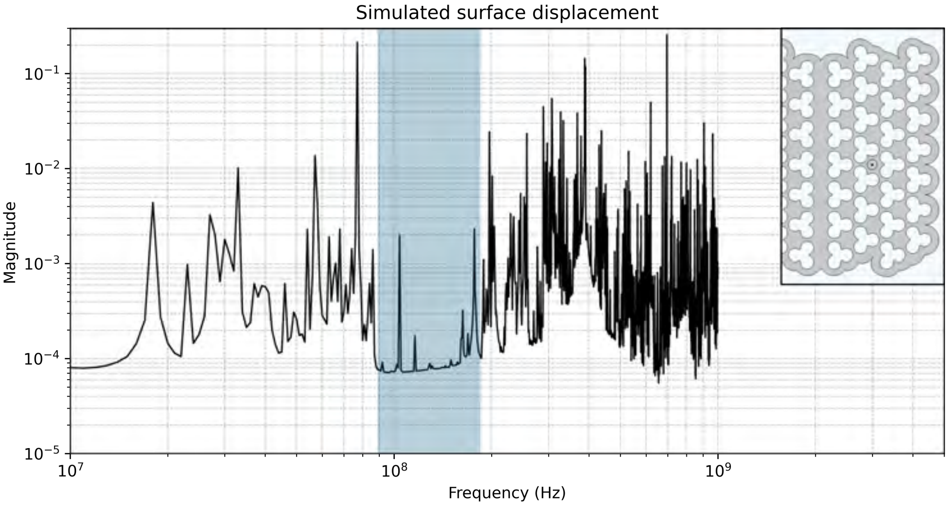

**Figure 38.** Simulated displacement of an island in the bulk PnC lattice of Y15 (1 MHz step-size). Blue area represents the possible phononic bandgap.

The above graph reveals a significant reduction in magnitude in the 88 MHz - 160 MHz range. This region, the bandgap, is highlighted in blue. At frequencies above the intial bandgap, there are various smaller frequencies ranges where the magnitude reduction is again significant. When comparing this surface average displacement with the band diagram for a $a = 24\mu m$ PnC lattice, these frequency ranges correspond with smaller bandgaps in the band diagram. This can be seen in Figure 39.

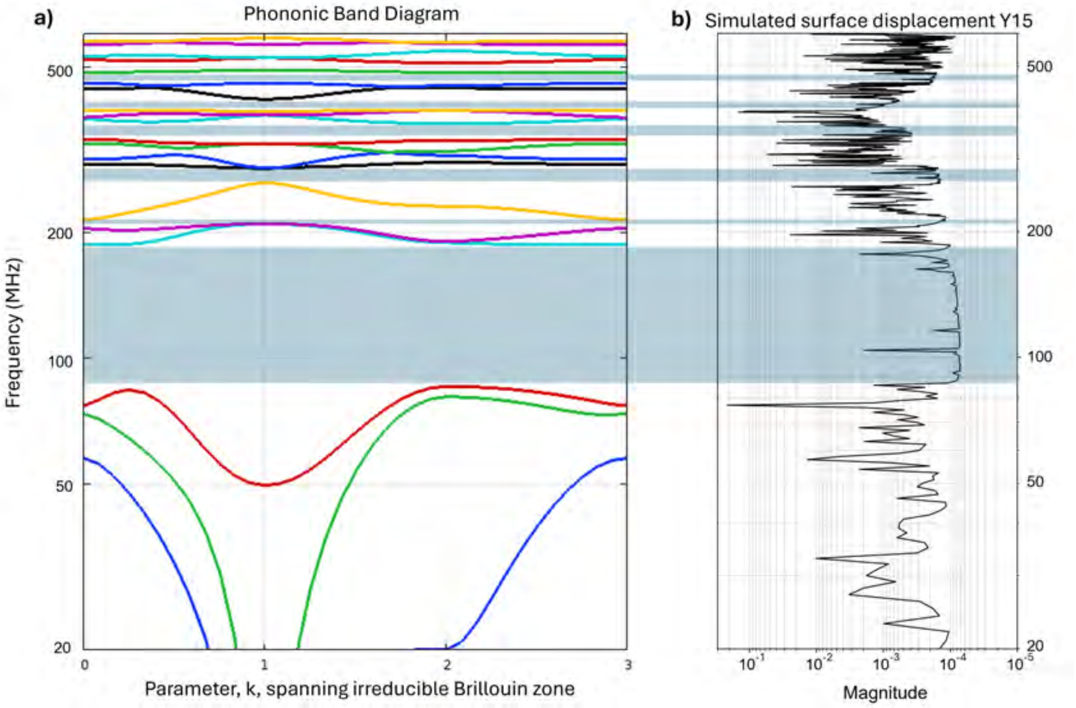

**Figure 39.** Phononic bandgap simulations of Y15. **a)** Phononic band diagram of infinitely periodic repeating unit cell of the PnC with lattice constant $a = 24\mu m$. **b)** Surface displacement simulation of Y15. The blue areas represent the bandgaps that are consistent in both graphs.

## 4.6 Surface Displacement Simulation of T12

The result of placing an overlapping point force excitation and surface average displacement on an island inside the bulk PnC lattice of T12 ($a = 10\mu m$) is expected to reveal the bandgap. For this simulation, a frequency range of 100 MHz - 10 GHz is modeled with a 100 MHz step-size (similar to the experiments). The result of this simulation is shown in Figure 40.

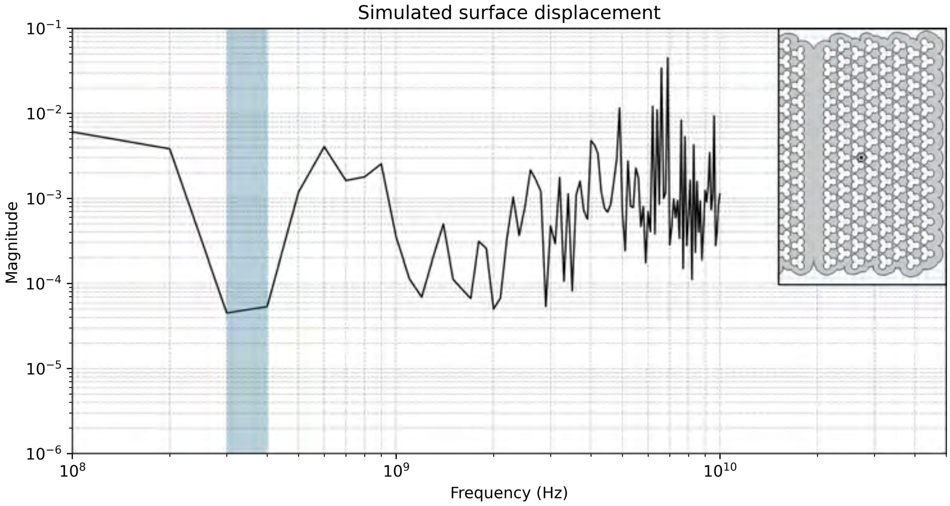

**Figure 40.** Simulated displacement of an island in the bulk PnC lattice of T12 (100 MHz step-size). Blue area represents the possible phononic bandgap.

In membrane T12, a bandgap should be clearly visible in the 250 MHz - 400 MHz range [9]. Even though there is a significant drop in magnitude visible at 300 MHz - 400 MHz, which is highlighted in blue, this drop only consists of two data points due to the 100 MHz step-size. To confirm that this drop in magnitude is the actual bandgap, the step-size is decreased to 5 MHz. The results of this refined simulation can be seen in Figure 41.

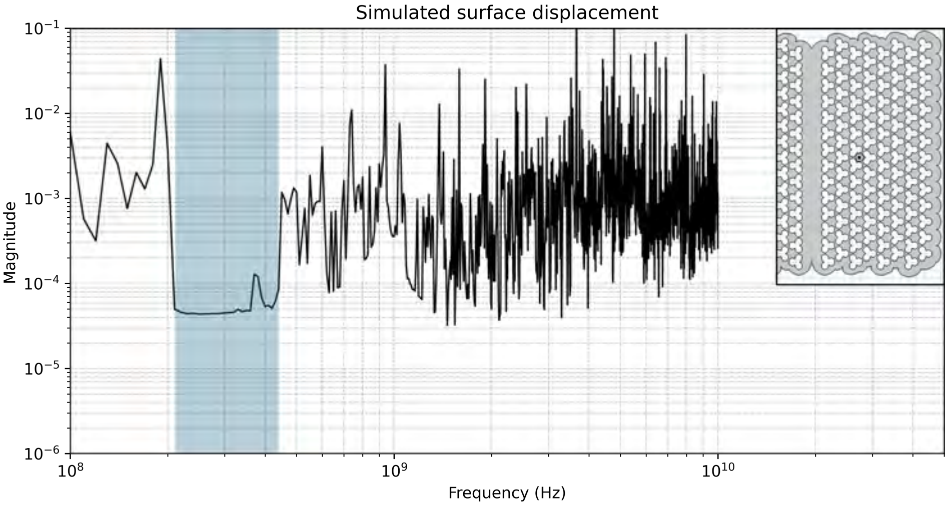

**Figure 41.** Simulated displacement of an island in the bulk PnC lattice of T12 (5 MHz step-size). Blue area represents the possible phononic bandgap.

In the graph above, a very clear drop in magnitude can be observed ranging from 210 MHz - 440 MHz . This confirms the formation of a bandgap in the bulk PnC lattice. Interestingly, at higher frequencies, more narrow drops in magnitude can be seen. When comparing this graph with the band diagram obtained for lattice constant $a = 10\mu m$ [9], these magnitude drops align with smaller bandgaps in the band diagram. This is shown in Figure 42.

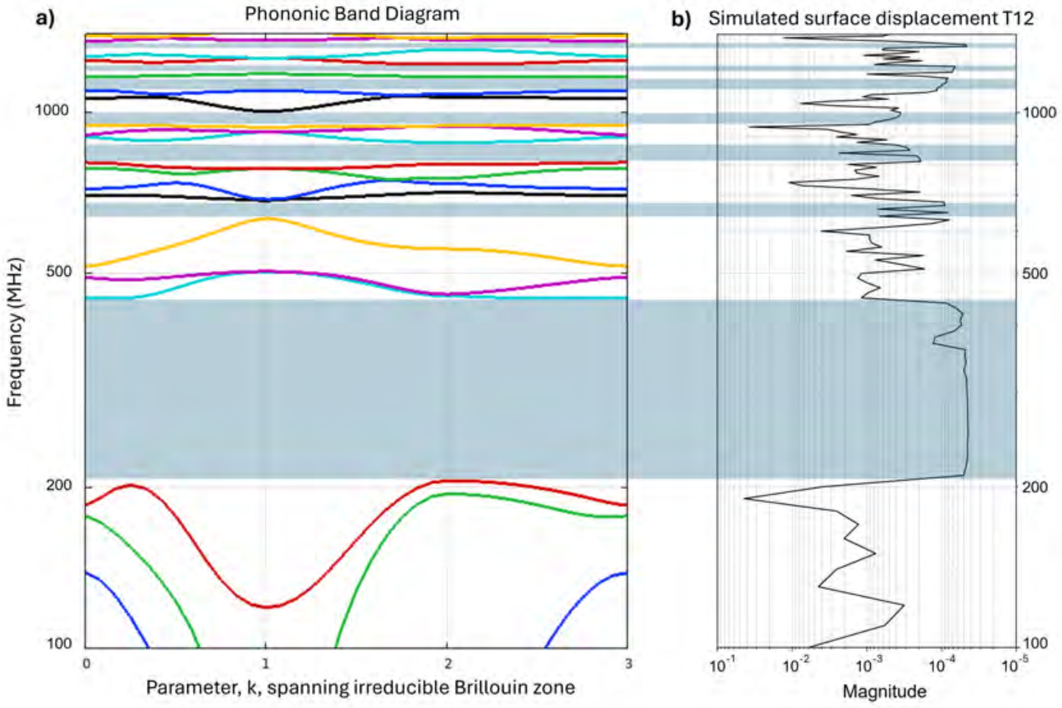

**Figure 42.** Phononic bandgap simulations of T12. **a)** Phononic band diagram of infinitely periodic repeating unit cell of the PnC with lattice constant $a = 10\mu m$. **b)** Surface displacement simulation of T12. The blue areas represent the bandgaps that are consistent in both graphs

## 4.7 Traveling Wave Simulations

Following the excitation of the rectangular beam, the simulation presented in Section 3.3 shows the generation of a longitudinal bulk waves propagation through the thickness of the beam. In the first nanoseconds, the bulk wave exhibits a nearly straight wavefront that slowly leads to the formation of a Lamb wave mode.

The propagation is analyzed by plotting the pressure distribution for a total of 100 ns, with time-steps of 5 ps. The pressure distribution at t = 0.005 ns reveals the generation of a longitudinal bulk wave right after excitation. This is shown in Figure 43. The angled sides of the bulk wave are a result of the coarse mesh that is used in the simulation. This mesh, the diagonal lines in the beam, is also shown in Figure 43. Simulations with a time duration of 10 ns where the mesh was finer, gave similar results (to the first 10 ns of the 100 ns signal) but drastically increased computational times. The dashed red line is the line segment on which the excitation is acting.

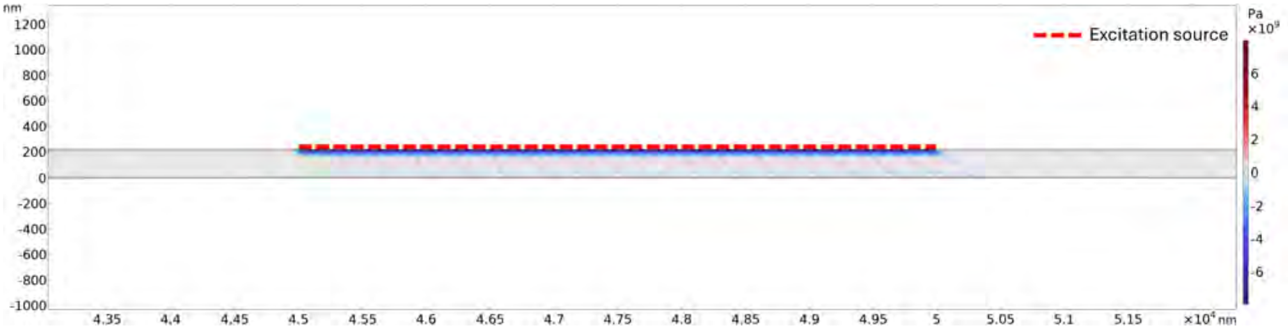

**Figure 43.** Simulated pressure field distribution in the cross-section of a rectangular beam at time t = 0.005 ns. The diagonal lines inside the beam are the mesh used in this simulation.

After traveling back and forth between the top and bottom of the beam multiple times, the pressure field starts to move in the horizontal direction. This propagation along the surface of the beam is the formation a Lamb wave. Figure 44 shows this lateral propagation at time t = 0.125 ns.

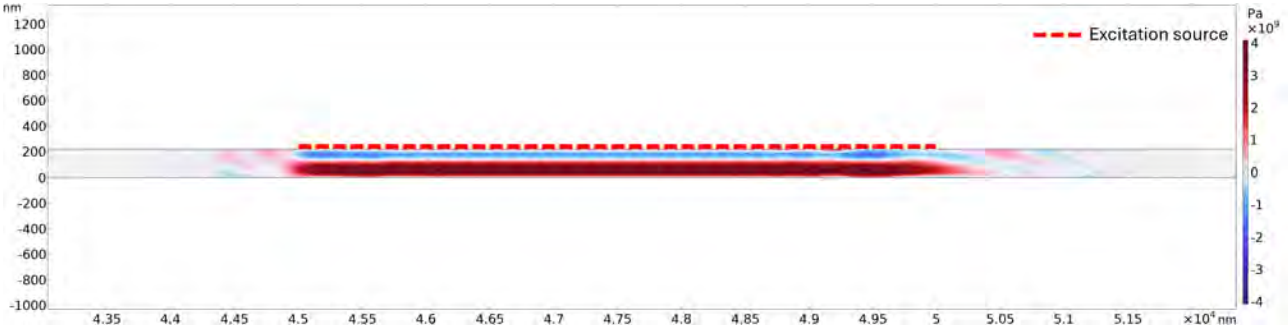

**Figure 44.** Simulated pressure field distribution in the cross-section of a rectangular beam at time t = 0.125 ns.

After approximately 2 ns, the first signs of lateral wave propagation reach the position of the boundary probe. This represents the arrival at the probe laser spot of the Lamb wave that formed from the initial bulk wave. The pressure distribution at this time is shown in Figure 45. The dashed black line is the line segment that acts as the boundary probe.

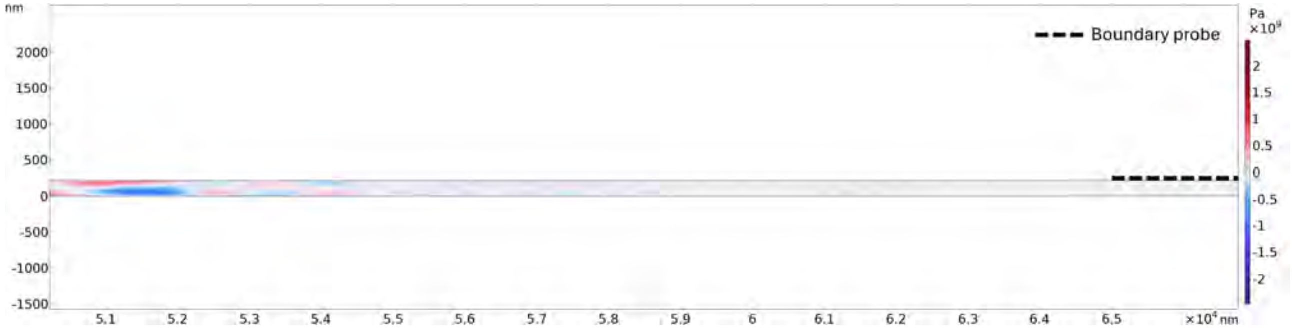

**Figure 45.** Simulated pressure field distribution in the cross-section of a rectangular beam at time t = 2 ns.

After around 13 ns, a stable propagation of the Lamb waves can be seen in the beam that reach the boundary probe. Figure 46 shows this clear establishment of Lamb waves for t = 13.585 ns.

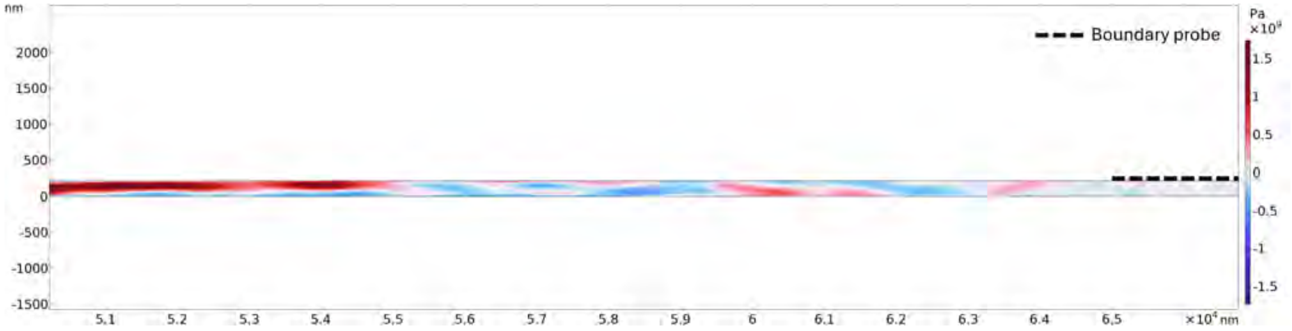

**Figure 46.** Simulated pressure field distribution in the cross-section of a rectangular beam at time t = 13.585 ns.

Finally, at t = 100 ns, the propagation of a Lamb wave along the full length of the cross-section can be seen, this is shown in Figure 47.

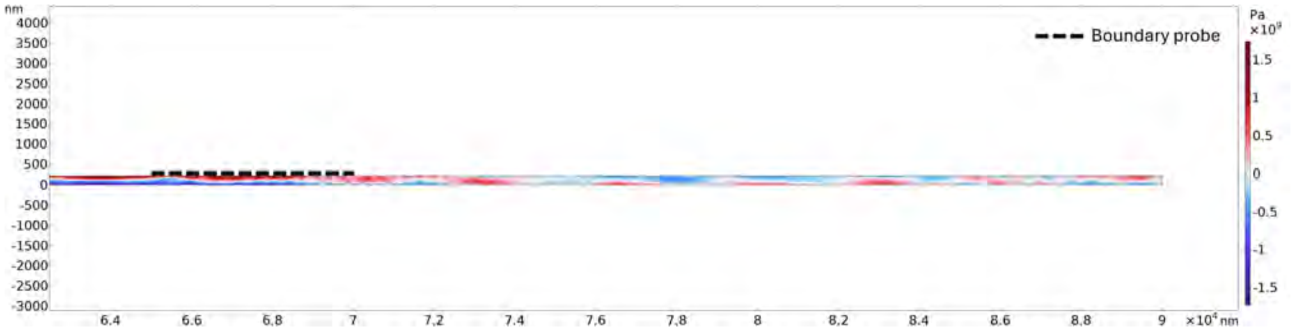

**Figure 47.** Simulated pressure field distribution in the cross-section of a rectangular beam at time t = 100 ns.

It is worth noting that the attenuation of the acoustic waves in these simulations are significantly lower than in reality. This is mainly due to the following reasons: The model does not contain the gold film that the sample contains. The material boundary between the $Si_3N_4$ and gold will likely attenuate the acoustic waves. The material boundary will likely also partially reflect the Lamb wave, which then results in extra modes. In addition to this, the COMSOL simulation assumes an undamped outer boundary of the beam. The experiments are not performed in vacuum and the membrane vibrations are subject to damping. However, this effect is expected to be relatively small.

The average pressure measured at the boundary probe can be plotted as a function of time to monitor the wave propagation. By converting this time-domain signal to the frequency domain, the FFT will show the dominant frequency of the generated Lamb wave. The result of this can be seen in Figure 48.

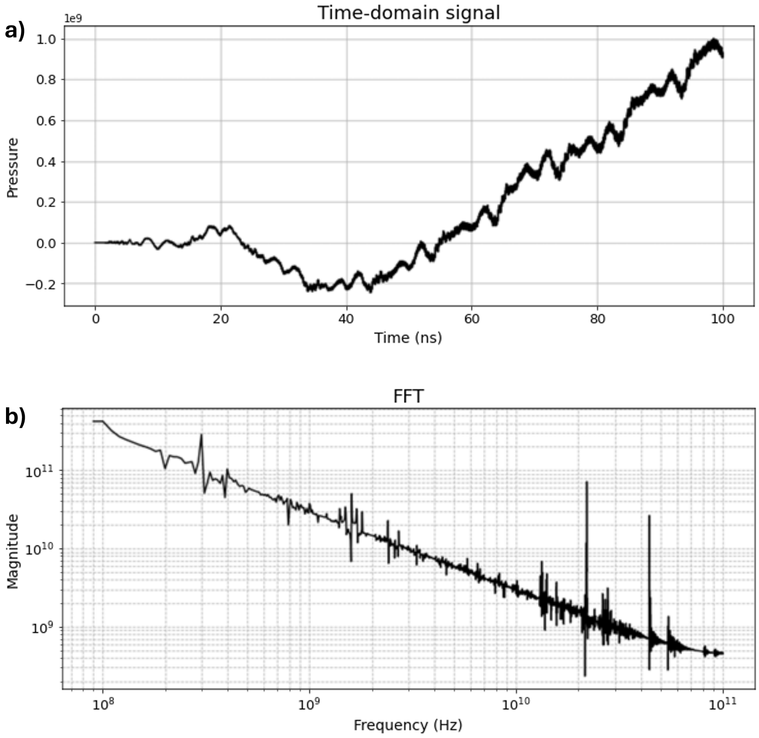

**Figure 48.** Resulting average pressure signal at the boundary probe. **a)** Time-domain signal. **b)** FFT. Dominant 300 MHz mode, which is the formed Lamb wave.

When looking at the FFT of the 100 ns time-domain signal, a dominant frequency component can be seen at 300 MHz. This corresponds to the Lamb wave that formed as a result of the initial bulk wave excitation.

## 4.8 Modes in the Substrate

By overlapping the pump laser with the probe laser on the substrate, the acoustic response at the point of excitation can be measured. Figure 49a shows the probe spot on the substrate. The blue circle serves as a reference to align the pump spot directly with the probe spot, ensuring optimal overlap and signal detection. Figure 49b shows the pump spot aligned with the blue reference circle, and thus the probe laser.

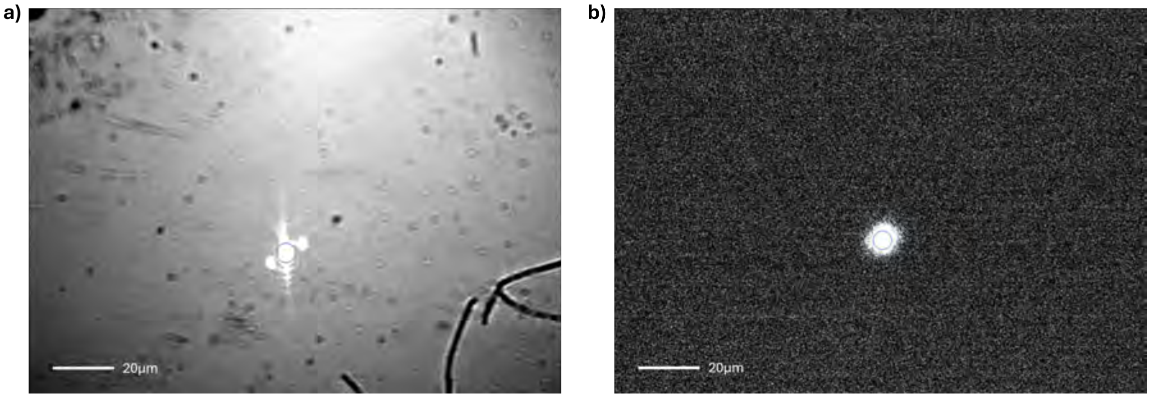

**Figure 49.** Sample images with positioning of the probe and pump laser. **a)** Probe laser spot on the substrate. **b)** Pump laser spot overlapping the probe laser spot. The blue circle serves as an alignment marker to overlap the pump with the probe.

The time-domain signal, along with its corresponding Fast Fourier Transform (FFT) resulting from this measurement is shown in Figure 50a and 50b respectively. Figure 50c presents the zoomed-in view of the same time-domain signal, showing only the first 1 ns to emphasize the dynamics of the substrate right after excitation. Figure 50d is the FFT of the 1 ns time-domain signal.

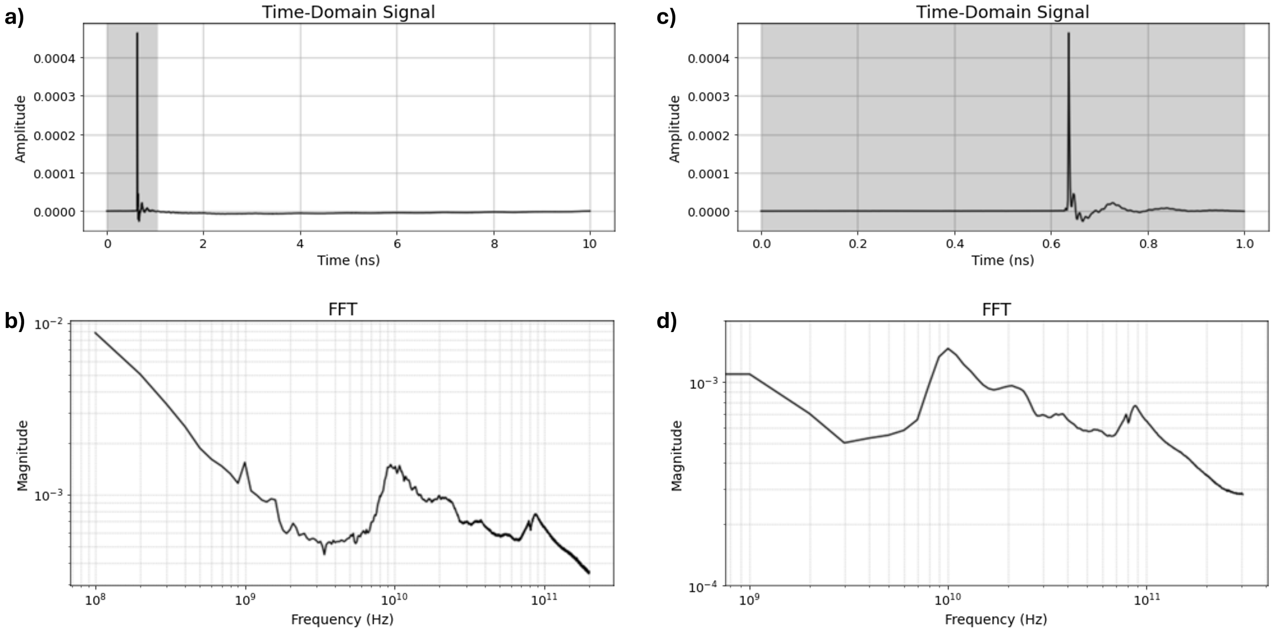

**Figure 50.** Resulting signal of an overlapping pump and probe on the substrate. **a)** Time-domain signal of the full 10 ns duration. **b)** FFT of the 10 ns signal. **c)** A 1 ns zoom in of the time-domain signal. **d)** FFT of the 1 ns signal.

When analyzing the FFT of either of the signals shown in Figure 50, a distinct 10 GHz and 85 GHz mode can be seen. One of these modes is likely a bulk acoustic wave (BAW) traveling back and forth between the thickness of the gold film. The frequency of such a longitudinal mode can be estimated by:

$$f_L = \frac{v_L}{2d} \tag{4}$$

where $f$ is the frequency, $v_L$ the longitudinal speed of sound in the material and $d$ the thickness of the film. Taking the frequency of 85 GHz and and a longitudinal sound velocity of 3250 m/s, would give a film thickness 19.1 nm. This fits the expected 20 nm thickness of the gold film. Therefore, the 85 GHz mode is very likely to be the longitudinal BAW in the gold film.

The 10 GHz mode is likely a shear mode in the gold film, of which the frequency can be estimated by :

$$f_S = \frac{v_S}{4d} \tag{5}$$

where now $v_S$ is the shear sound velocity in gold of 1040 m/s [43]. Keeping the thickness $d$ at 20 nm, would result in a $f_S$ of 13 GHz. This strongly suggest that the 10 GHz mode is a shear mode in the gold film.

In addition to these mechanical modes, the FFT also contains a notable peak at exactly 1 GHz. This peak is present in every measurement, even when the pump laser is turned off. This artifact is likely from an external or electric source and is therefore disregarded in the analysis.

## 4.9 Modes in the Suspended Membrane

The measurements performed on the suspended membranes contain substantial more modes that the measurements on the substrate. This results in more complex FFTs that contain eigenmodes of the membrane, modes in the gold film, modes in the $Si_3N_4$, hybrid modes in both the $Si_3N_4$ and the gold film, but also the traveling waves. Characterizing all the different modes would be to complex to fit into the scope of this MSc thesis, so the focus of this section is to see how the 300 MHz Lamb wave (found in Section 4.7) behaves on different suspended membranes.

### 4.9.1 Membrane T12 without AOM

An important step is to distinguish the traveling wave modes from the eigenmodes of the membrane. In an effort to accomplish this, a measurement is done where the probe laser is in a fixed position and the pump laser is moved along the membrane. Doing this, the eigenmodes of the membrane should be visible in each measurement with roughly the same order of magnitude. The modes that reduce in magnitude when the pump move to a larger distance should then be the traveling waves. If these traveling waves are inside the bandgap of the PnC lattice, the mode should significantly reduces when the pump is placed in the PnC lattice. This measurement is done on T12 for distances $d = 20\mu m$, $d = 50\mu m$ and $d = 80\mu m$ between the pump and the probe spot and placing the pump in the PnC lattice. A schematic is shown in Figure 51.

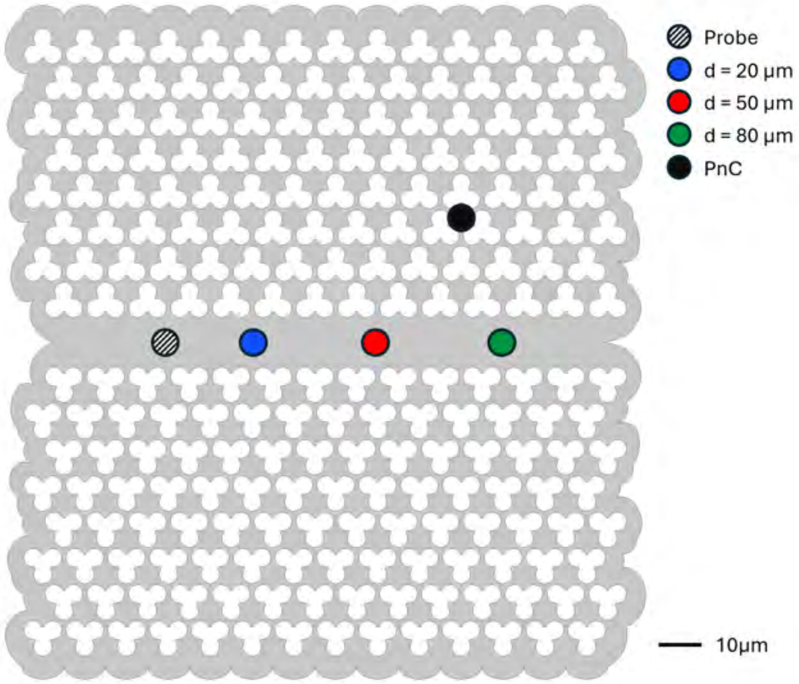

**Figure 51.** Locations of the probe spot with respect to the pump spot, for the measurements on performed on membrane T12 and S11.

The results of doing this for distances $d = 20\mu m$, $d = 50\mu m$ and $d = 80\mu m$ between the pump and the probe spot are shown in Figure 52. A measurement where the pump is placed in the bulk PnC lattice at a distance of approximately $d = 80\mu m$ from the probe is also included.

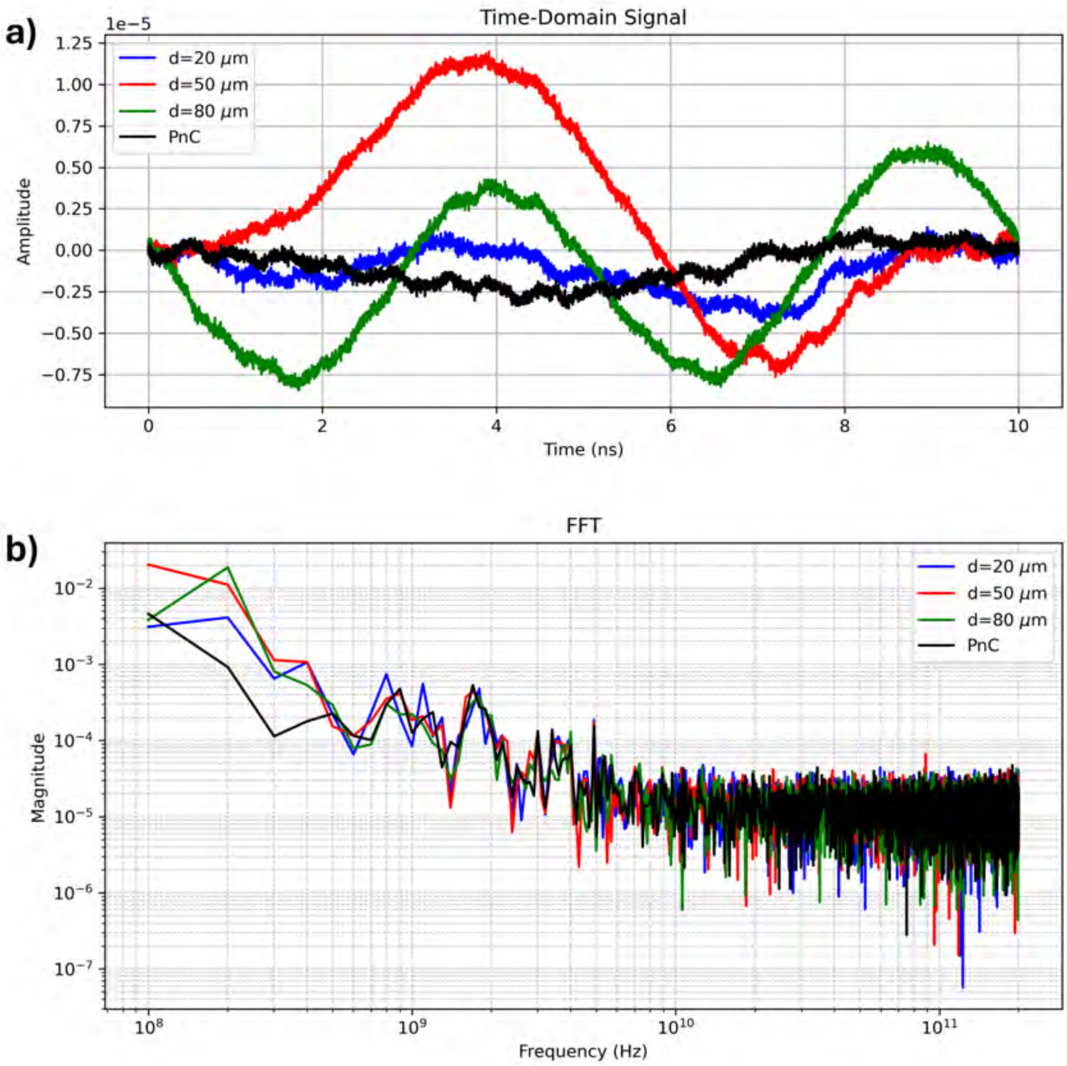

**Figure 52.** Result of the measurements performed on T12. **a)** Time-domain signal. **b)** FFT. The magnitude of the 300 MHz mode reduced is by roughly a factor 10 when the pump is placed in the PnC lattice.

The graph above shows clear modes that remain nearly constant across all measurements, like the modes at 800 MHz, 1.8 GHz and 5 GHz. The most interesting is the 300 MHz mode, since the amplitude varies across the measurements in the waveguide and drops a factor 10 in magnitude when the pump is placed in the Pnc lattice. This could be an indication that the 300 MHz mode is a traveling wave, since the bandgap of this membrane is 210 MHz - 440 MHz.

An important observation is the increase in magnitude of the 300 MHz mode when increasing the distance from $d = 50\mu m$ to $d = 80\mu m$. Since the distance increases, the energy loss of the traveling wave is expected to decrease. A possible explanation for this, is that the spotsize of the pump laser is nearly the same size as the width of the waveguide. It can happen that the pump laser was not perfectly on the waveguide for the $d = 50\mu m$, but it was more on the waveguide for the $d = 80\mu m$. The latter measurement would result in more energy for the traveling wave and thus a higher magnitude.

Another important note is that the time range of the signal is 10ns, this means the resolution of the FFT is 100 MHz. Concluding that the 300MHz mode is a traveling wave, is therefore probably not correct, since there are likely multiple modes between the 200 MHz and 400 MHz range. Unfortunately, these modes can not yet be resolved.

### 4.9.2 Membrane T12 with AOM

With the addition of the AOM, like discussed in Section 3.7, the time-domain signal is increased to 20 ns. With this increase, the resolution of the FFT goes up to 50 MHz. This should reveal a possible bandgap of the membrane more clearly. To validate this, the measurement shown in Figure 51 is repeated. The distances of the pump laser with respect to the probe laser are kept as similar as possible. The result of this improved measurement can be seen in Figure 53.

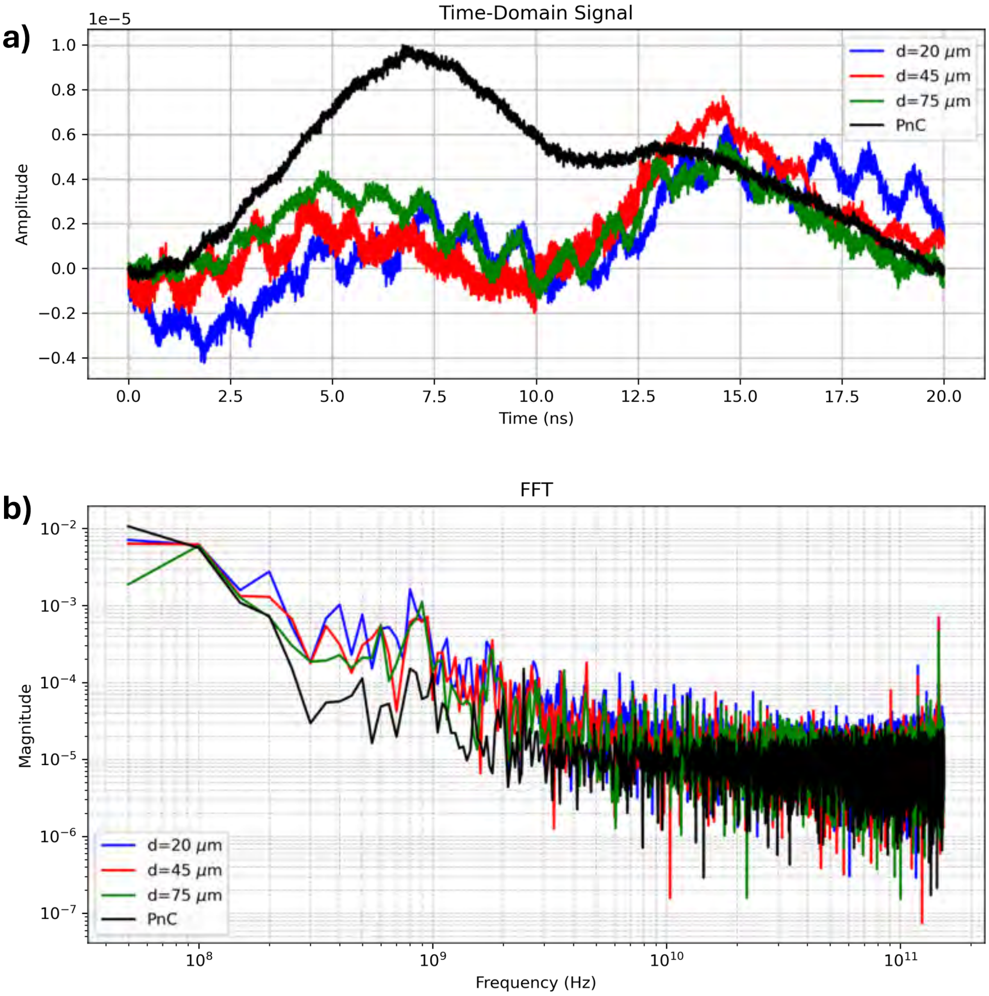

**Figure 53.** Result of the measurements performed on T12 with the added AOM. **a)** Time-domain signal. **b)** FFT. The 300 MHz mode is again reduced by roughly a factor 10 when the pump is placed in the PnC lattice.

Similar to the measurement without the AOM, a significant magnitude drop is seen at 300 MHz when the pump laser is placed in the bulk PnC lattice. This is an ever stronger indication that the 300 MHz Lamb wave is confined to the waveguide of T12.

### 4.9.3 Membrane S11 with AOM

The measurements performed in Section 4.9.2 are repeated on membrane S11. This membrane is nearly identical to T12, but has a lattice constant of $a = 15\mu m$ and a corresponding phononic bandgap of 150 MHz - 265 MHz. The location of the probe laser and the distances of the pump laser are again kept as similar as possible to the previous measurements. The resulting time-domain signal and FFT are shown in Figure 54.

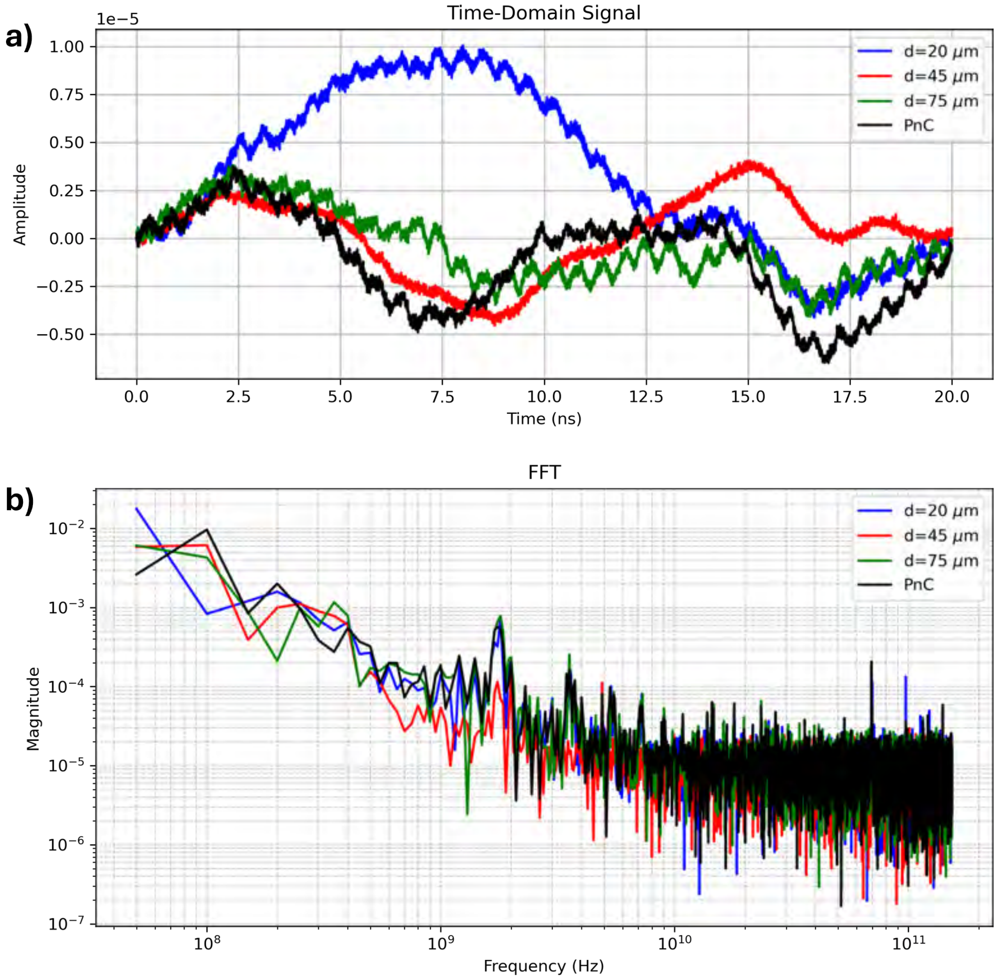

**Figure 54.** Result of the measurements performed on S11 with the added AOM. **a)** Time-domain signal. **b)** FFT. Here the 300 MHz mode is nearly consistant, even when the pump is placed in the PnC lattice.

In the FFT, no significant drop can be seen at 300 MHz when placing the pump in the PnC lattice. This is expected, since the Lamb wave of 300 MHz is outside the bandgap of membrane S11 and the PnC lattice now supports this mode. However, this is an even stronger indication that the Lamb wave is actually confined to the waveguide in membrane T12 and not in membrane S11. There a significant magnitude drop is seen at 300 MHz when the pump is located in the PnC lattice (Figure 52 and Figure 53).

## 4.10 Comparison of COMSOL with Measurement

The surface displacement simulations performed in Section 4.5 and Section 4.6 can also be done with a 'pump' and 'probe' that are not overlapping. With this, we can recreate the measurement performed in Section 4.9.2. The point excitation is placed in the PnC lattice on the same island as the pump laser in the measurement. The surface average displacement in positioned inside the waveguide at the same location as the probe laser in the measurement. The resulting surface displacement across the frequency domain can be seen in Figure 55.

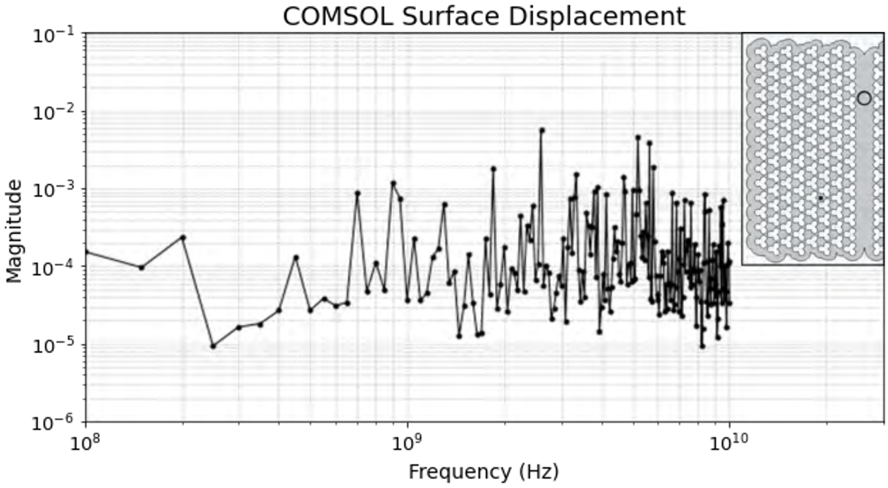

**Figure 55.** Surface average displacement of the 'probe laser' (black circle) in the waveguide, due to the point force of the 'pump laser' (black dot) in the PnC lattice.

The result of the above graph looks similar to the measurement performed on this membrane that was shown in Section 4.9.2. However, the most prominent dip that can be seen in Figure 55 is not at 300 MHz, but at 250 MHz. This is most likely caused by the fact that the membrane in the simulation has a thickness of 200 nm, while the actual membrane has a thickness of 220 nm. When scaling the result of the COMSOL simulation with 10% and overlapping it with the result from the measurement, Figure 56 is obtained.

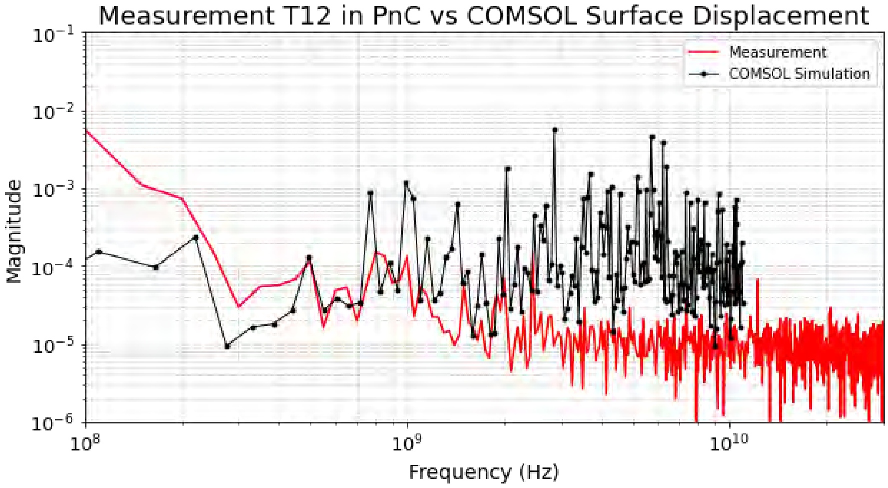

**Figure 56.** Measurement on T12 with the pump in the PnC lattice and the probe in the waveguide in red. Corresponding COMSOL simulation in black.

The frequency of the modes of the COMSOL simulation roughly correspond to the modes seen in the measurement. The main difference is the decay in the measurement, that is not in the COMSOL simulations.

However, these simulations only correspond to the measurements when the pump and probe are placed at a large enough distance ($\gtrsim 50\mu$m). When the pump and probe are overlapping, these simulations are not able to get a correct displacement across the frequency spectrum. Figure 57 shows two measurements (in red) with the corresponding simulations (in black), where the small square indicates the pump position and the circle indicates the probe position. In Figure 57a the pump and probe are overlapping and in Figure 57b, the pump and probe are placed at a distance of $70\mu$m. In addition to this, Figure 57b has a blue curve where the frequencies of the COMSOL simulation are scaled by a factor 1.2. This scaling of 20% is needed to have overlap in the 1-5 GHz range.

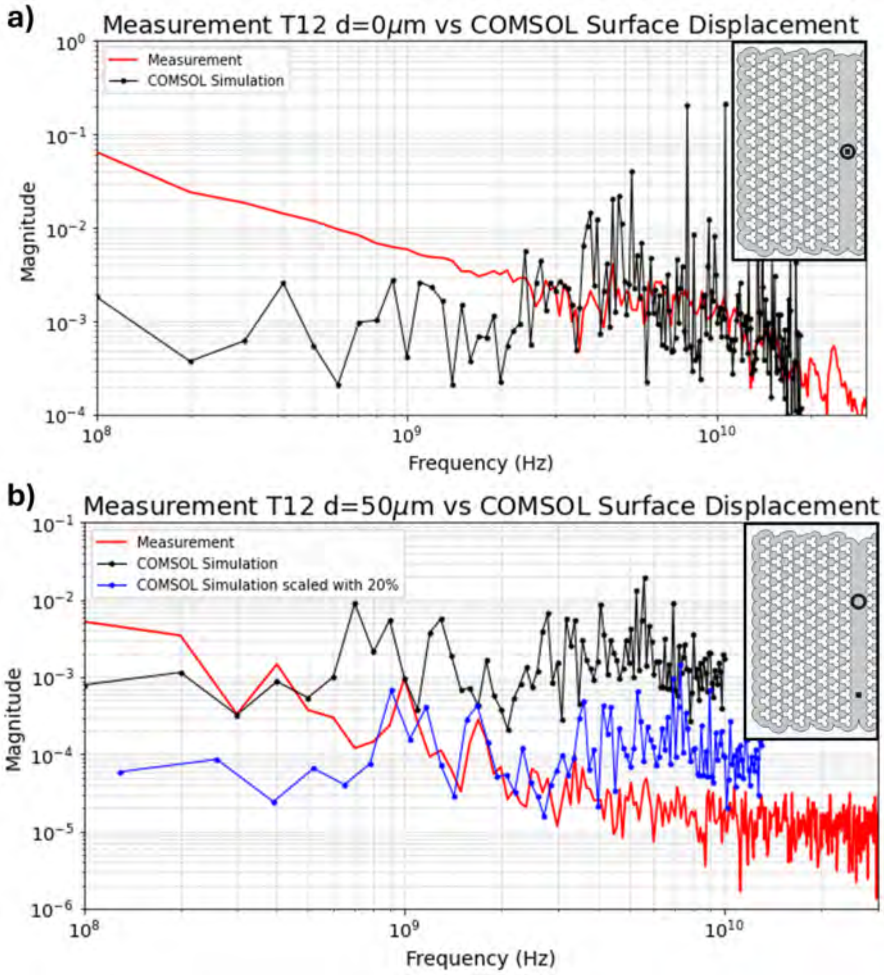

**Figure 57.** Measurements compared with COMSOL simulations. **a)** Overlapping pump and probe on membrane T12. The measurement is in red and the simulation in black. **b)** Distance of 50 $\mu$m between pump and probe. The measurement is in red and the simulation in black. The blue curve is the same COMSOL simulation, but now scaled with 20%.

In Figure 57a, the measurement shows almost no modes up to 1 GHz. In the COMSOL simulation, there are multiple modes below this frequency. A possible explanation for this is that at low frequencies, the photoacoustic signal is dominated by the thermal contribution. Above the 1 GHz, only a few few similarities can be seen, like the dip at 3.5 GHz for example. This might be caused by BAWs and SAWs that reflect of the material boundaries and PnC boundaries respectively. These waves interfere with eachother and cause all type of hybrid modes.

In Figure 57b, the low frequency (100 MHz - 500 MHz) modes closely match the COMSOL simulation. To have the higher frequencies (500 MHz - 2 GHz) matching the measurement, the frequencies of the COMSOL simulation have to be scaled by a factor 1.2. For higher frequencies (like the dip at 3 GHz), the COMSOL simulation has to be scaled even more. This might be an indication that the stress redistribution is different in the actual membrane, than in the simulation. The overall spectrum has the same trend in both the simulation and measurement. The frequencies at which these modes occur seem to increase for higher frequencies.

## 4.11 Laser-Induced Membrane Damage

Right after performing a measurement where the pump laser was used on either a membrane or the substrate, clear discolorations were visible on the camera inside the set-up. On the substrate, white discs larger than the spot size of the pump laser with a darker inner circle can be seen. This darker inner circle is like molten due to the laser, where the surrounding white disc is the heated area [44] [45]. These discs are shown in Figure 58a. In the waveguide on the other hand, the discolorations due to the pump laser resulted in darker spots equal to the spot size of the pump laser. This is likely only molten gold and is shown in Figure 58b.

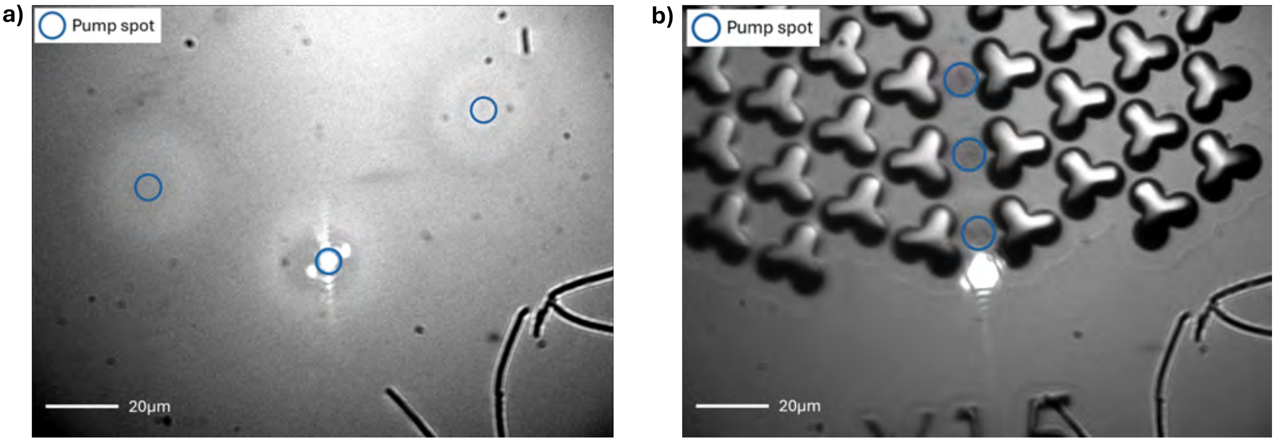

**Figure 58.** Discolorations visible on the camera inside the setup. **a)** Lighter discs larger than the spot size on the substrate. **b)** Darker spots equal to the spot size inside the waveguide. The blue circles indicate the location and and spot size of the pump laser.

These discolorations are further investigated by placing the sample in the white light interferometer (WLI). This revealed that the surface of the sample is altered due to the interaction with the pump laser. On the substrate the same discs that could be seen on the camera, are clearly visible in the WLI (Figure 59a). However, the surface of the substrate remains relatively flat. In the waveguide, the interaction with the pump laser resulted in craters that are a tens of nanometers deep (Figure 59b).

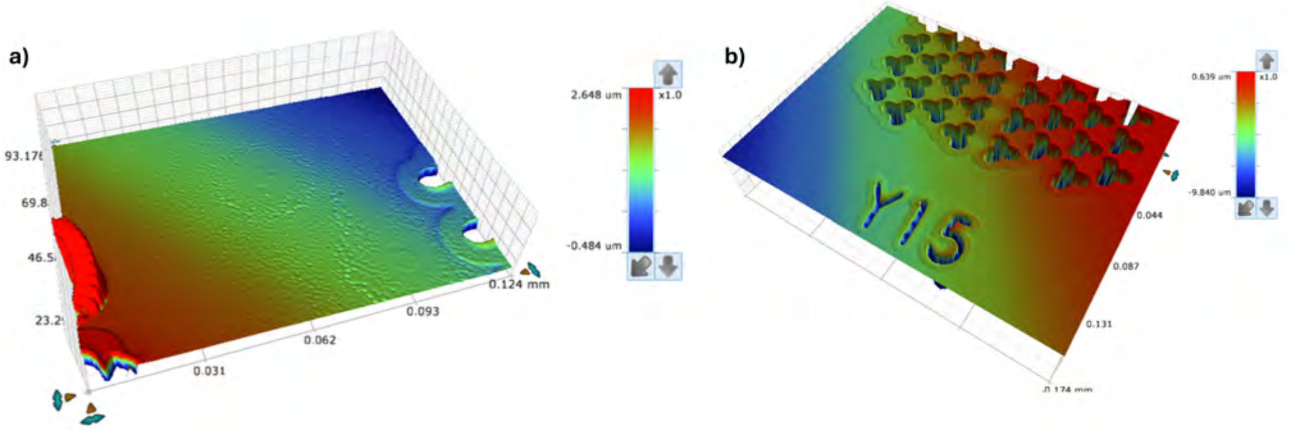

**Figure 59.** White light interferometer images showing laser-induced damage. **a)** Visible discs larger than the spot size on the substrate. **b)** Visible crates equal to the spot size inside the waveguide.

The effect of these altered surface properties is investigated by first doing a measurement on an unused part of the waveguide. Then the exact same measurement is done on the altered surface, without moving the lasers or the sample. This way, the direct effect of the surface alteration on the measurement signal can be seen. The two signals resulting from this experiment are shown in Figure 60. Here the black signal is measured on an unused part of the waveguide and the red is the subsequent measurement.

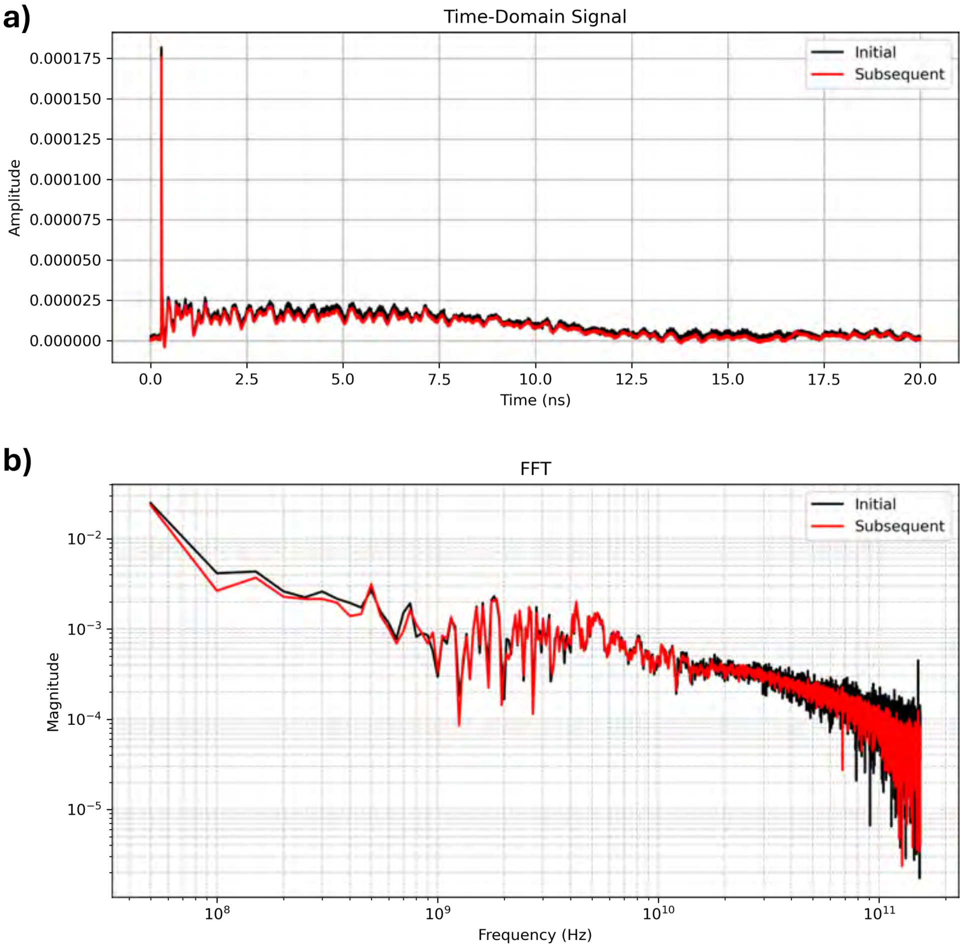

**Figure 60.** Resulting signals of two subsequent measurements. The black signal is on an used part of the waveguide, the red signal is on the same location that now has an altered surface. **a)** Time domain signal. **b)** FFT.

In Figure 60, the black curve shows the result of a measurement done on an unused section of suspended membrane T12. The red curve shows the result of the same measurement, done on the section used before. The trend of both the measurements is nearly identical, other than the fact that the signal of the second measurement slightly lower in magnitude.

The measurements done in Figure 60 were performed with an active pump laser of around 10 minutes each. When increasing the time that the pump laser is active, a larger drop in the signals magnitude is seen. However, the overall shape of the signal remains the same. This indicates that the measurements are repeatable and because of this, the surface alteration is ignored for all the measurements.

With the implementation of the AOM, the laser-induced damages of the gold film is observed to be (nearly) eliminated. Figure 61 shows the state of the membrane after a measurement where the AOM was used, the red circle indicates the location of the pump laser and the blue circle indicates the location of the probe laser. The white circles indicate laser-induces damage from previous measurements without the AOM. The island where the pump was placed shows no signs of discoloration.

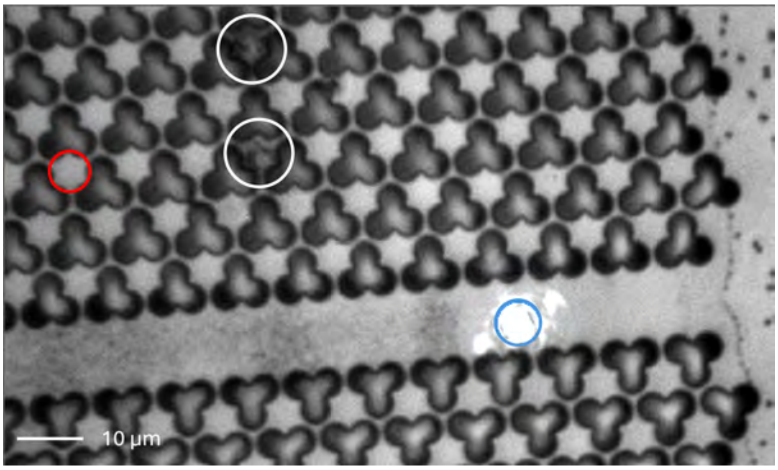

**Figure 61.** No laser-induced damage is visible at the location of the pump laser (red circle) after the measurement. The white circles indicate damage from previous measurements where no AOM was used. The blue circle is the location of the probe laser.

Since the AOM blocks half of the pulses, the membrane has twice the amount of time to dissipate the heat between the pulses. In addition to this, laser power is lost in the AOM, resulting in a less heating of the gold film. This gives an indication of the temperature that the gold film might reach. Without the AOM, a temperature of >1064°C is reached and with the AOM this reduces to <1064°C. Where 1064°C is the melting point of gold.

# 5 Discussion

This section will discuss, compare and analyze the results obtained in this thesis. In addition to this, recommendations for future steps on this topic are presented.

## 5.1 Membrane Y15 vs T12

Simulations of both membrane Y15 and T12 show the formation of clear bandgaps around the expected frequencies. The eigenmodes of both membranes show a clear reduction in number modes for the frequencies corresponding with the expected bandgap. For the modes that still exist inside the expected bandgap, the out-of-plane displacement is localized along the edges of the membrane or inside the waveguide. The bulk PnC lattice shows little to no displacement.

Plotting the surface average displacement of the PnC lattice due to a point force, shows the same results. Around the expected bandgap, a clearly lower magnitude of displacement is seen. For membrane T12, this reduction in magnitude is very clean (only one mode inside the bandgap). Membrane Y15 has more modes that are still observed in the bandgap. This can be explained by the fact that the PnC lattice is only four crystals deep (w.r.t. 8 crystals on T12). Some modes leak a few crystals deep into the PnC lattice and can therefore still be observed. Making a wider PnC lattice and measuring deeper into the PnC lattice would likely result in a cleaner bandgap.

The comparison of eigenmodes measured on the laser interferometer and the COMSOL simulations, show notable more deviations for Y15 than for T12. After investigating membrane Y15 further, it was seen that the membrane is not successfully suspended. The waveguide was still connected to the substrate by a number of pillars. These pillars influence the behavior of the membrane and therefore the resonance frequencies. Membrane T12 still showed deviations between the measurements and COMSOL simulations. These are attributed to simplifications made in the model.

## 5.2 Traveling Wave

The simulation performed in Section 3.3 showed that the longitudinal bulk wave results in a 300 MHz Lamb wave traveling in the lateral direction. The attenuation of this simulated Lamb wave is likely lower then in the actual membranes. This is because at the interface of the gold film and the $Si_3N_4$, energy loss is expected. On the other hand, the mismatch between the thermal expansion coefficients of gold and $Si_3N_4$ can lead to larger excitation than the input signal used for these simulations.

This attenuation can be further investigated by integrating the gold layer into the COMSOL model. Using the multiphysics coupling of COMSOL, this photo-thermal excitation can be modeled. However, this drastically increased the computation time and was not possible in this thesis due to time constraints. The frequency of the resulting Lamb wave is not expected to change much, since this is mainly dependent on the thickness of the beam.

## 5.3 Wave Confinement

Membrane T12 shows clear signs of confining the Lamb wave to the waveguide. The frequency of the Lamb wave (300 MHz) shows a factor 10 drop in magnitude when the pump laser is place in the PnC lattice, compared to when it is placed inside the waveguide. Since the bandgap of this membrane is 210 MHz - 440 MHz, a traveling wave of 300 MHz should be blocked by the PnC lattice. On membrane S11, with a bandgap of 150 - 265 MHz, this drop at 300 MHz is not seen when the pump is placed in the PnC lattice. This is in line with expectations, as the bandgap does not block traveling waves of 300 MHz. This strongly suggests that the 300 MHz is indeed a traveling (Lamb) waves, that is blocked by the PnC lattice of T12, but not by the PnC lattice of S11.

## 5.4 Laser-Induced Damage

The laser-induced damage on the sample is likely the (partial) melting of the 20 nm gold film. The melting of the gold is seen to be more extreme on the suspended membranes, than on the substrate. This is because on the substrate, the heat can dissipate through the Si. In the suspended waveguide, this Si is etched away.

With the introduction of the AOM, the laser-induced damage is (almost) fully eliminated. The AOM blocks half of the pulses, so the gold layer has twice the amount of time to dissipate the heat. This seems to be enough time to keep the temperature below the melting point of gold (1064°). In addition to this, minor losses in the AOM result in less heating of the sample.

## 5.5 Future Steps

During the measurements performed in this thesis, multiple challenges were encountered. This subsection discussed the encountered challenges with possible solutions to improve the performance of the membranes. The improvements are mainly related to the design of the PnC lattice and the metal film on the sample.

### 5.5.1 PnC Lattice Design

One significant challenge is related to the suspended waveguides with lattice constants smaller than $a = 10\mu m$. In these configurations, the 'islands' in the PnC lattice and the width of the waveguide itself are too small to fit the pump and probe laser spots on. This results in such low reflection of the probe laser, that measurements are not possible.

A potential approach to overcome this limitation is by increasing the width of the waveguide to provide more surface area for both lasers. In addition to this, specially designed islands can be incorporated in the PnC lattice to serve as a point of measurement/excitation. However, these islands may alter the phononic bandgap if the PnC lattice is not large enough to maintain its original properties. Therefore, any design adjustments should be accompanied by simulations and experimental verification to ensure the formation of the desired bandgap.

### 5.5.2 Metal Film

The laser-induced damage of the gold film suggest that replacing the gold coating with another thin metal film could improve robustness and performance of the suspended waveguides. Samples with a aluminum coating of equal thickness did not exhibit this damage in comparable measurements, despite have a lower melting point (660°C for aluminum and 1064°C for gold). This indicates that properties like absorption of the laser wavelength, film adhesion to the substrate and thermal conductivity play a role in the damage threshold. It is advisable to investigate alternative thin metal films that can replace the current gold film.

### 5.5.3 Simulations

The simulations performed in this thesis can be extended and improved to gain further insight in the behavior of the waveguides. The most obvious improvements are the addition of the thin gold film and adding a photo-thermal excitation, instead of a force excitation.

Another relevant extensions would be to change the spot size in the simulation where the frequency of the Lamb wave is determined. This might give a direct relation between the spot size and the frequency of the Lamb wave, which can be used to excite Lamb waves in the bandgap of certain membranes.

# 6 Conclusion

In this thesis, extensive simulations of two different suspended waveguides (Y15 with $a = 24\mu m$ and T12 with $a = 10\mu m$) successfully showed the existence of a bandgap in the bulk PnC lattice. An absence of eigenmodes localized inside the PnC lattice was found for the frequency ranges that correspond with the bandgaps of the phononic band diagrams. This confirms that the PnC lattices of the membranes behave like an infinite periodic lattice of suspended PnCs.

Notable deviations were found between the results obtained using the laser interferometer setup and the COMSOL simulations. For Y15, these large deviations can mainly be explained by the fact that the waveguide is not fully suspended. The pillars beneath the waveguide influence the behavior of the membrane. For T12, more similarities were seen. The simplifications made to conduct the model still lead to deviations.

The experiments showed the presence of traveling waves on the substrate. A longitudinal mode, the bulk acoustic wave, propagating back and forth between the top and bottom surface of the gold film is seen. In addition to this, a shear mode in the gold film was observed. Both of these modes decayed quickly and were only present in the first 2 ns of the signal.

Simulations confirmed the formation of a 300 MHz Lamb wave as a result of the longitudinal bulk wave. Membrane T12, that has a phononic bandgap of 210 MHz - 440 MHz, showed a factor 10 reduction of this 300 MHz mode when the pump laser was placed in the PnC lattice, compared to when it was placed in the waveguide. For membrane S11, that has a bandgap of 150 MHz - 265 MHz, this reduction was not observed when the pump laser was placed inside the PnC lattice. This strongly suggest that the 300 MHz Lamb wave is confined to the waveguide for membranes that have a bandgap where this mode falls within.

The simulations are able to roughly recreate the modes in the membrane across the frequency spectrum, when the pump and probe are not overlapping. The scaling of this spectrum needs to be adjusted to correctly overlap all the modes.

Laser-induced damage was observed when the pump laser was placed on the sample without using the AOM. The main effect of this damage was lower amplitude of the resulting signal. Since the trend of the signal stays nearly identical, this damage was not further investigated. Introducing the AOM into the setup eliminated the laser-induced damage to the sample.

The introduction of the AOM also allowed us to repeat the measurements with a higher frequency resolution (50 MHz instead of 100 MHz), while showing the same confinement of the 300 MHz Lamb wave on membrane T12. This also showed the reproducibility of the measurements.

# References

[1] Carlos Errando-Herranz et al. "MEMS for Photonic Integrated Circuits". In: *IEEE Journal of Selected Topics in Quantum Electronics* 26.2 (Mar. 2020). ISSN: 15584542. DOI: 10.1109/JSTQE.2019.2943384.

[2] Sarah Benchabane and Alexandre Reinhardt. *8 Elastic Metamaterials for Radiofrequency Applications*. Tech. rep. Aug. 2019.

[3] Sophie Weiyi Ding et al. "Integrated phononic waveguides in diamond". In: *Physical Review Applied* 21.1 (Jan. 2024). ISSN: 23317019. DOI: 10.1103/PhysRevApplied.21.014034.

[4] R. Lucklum et al. "A3.1 - Phononic Crystals and Applications". In: AMA Service GmbH, Dec. 2020, pp. 62–67. DOI: 10.5162/sensor2013/a3.1.

[5] Wei Fu et al. "Phononic integrated circuitry and spin–orbit interaction of phonons". In: *Nature Communications* 10.1 (Dec. 2019). ISSN: 20411723. DOI: 10.1038/s41467-019-10852-3.

[6] Felix M. Mayor et al. "Gigahertz Phononic Integrated Circuits on Thin-Film Lithium Niobate on Sapphire". In: *Physical Review Applied* 15.1 (Jan. 2021). ISSN: 23317019. DOI: 10.1103/PhysRevApplied.15.014039.

[7] Thomas Vasileiadis et al. *Progress and perspectives on phononic crystals*. Apr. 2021. DOI: 10.1063/5.0042337.

[8] Maximiliaan Van Der Vis. *Designing a Suspended Silicon Nitride GHz Acoustic Beam Splitter*. Delft, Jan. 2023.

[9] András Soltesz. *Engineering and tuning GHz SAWs in suspended SiN membranes*. Delft, June 2024.

[10] Martin Robin et al. "Conoscopic interferometry for optimal acoustic pulse detection in ultrafast acoustics". In: (Nov. 2022). URL: http://arxiv.org/abs/2211.03145.

[11] Vincent Laude and V Laude. *Principles and properties of phononic crystal waveguides*. Tech. rep. URL: https://hal.science/hal-03360024v1.

[12] R. H. Olsson and I. El-Kady. "Microfabricated phononic crystal devices and applications". In: *Measurement Science and Technology* 20.1 (2009). ISSN: 13616501. DOI: 10.1088/0957-0233/20/1/012002.

[13] A. Khelif et al. "Guiding and bending of acoustic waves in highly confined phononic crystal waveguides". In: *Applied Physics Letters* 84.22 (May 2004), pp. 4400–4402. ISSN: 00036951. DOI: 10.1063/1.1757642.

[14] Chi Zhang, Qiang Liu, and Zhengbiao Ouyang. "Band Gap Optimization for GHz Elastic Waves in Gold Phononic Crystals". In: *IOP Conference Series: Materials Science and Engineering*. Vol. 585. 1. Institute of Physics Publishing, Aug. 2019. DOI: 10.1088/1757-899X/585/1/012051.

[15] C. Croënne et al. "Band gaps in phononic crystals: Generation mechanisms and interaction effects". In: *AIP Advances* 1.4 (Dec. 2011). ISSN: 21583226. DOI: 10.1063/1.3675797.

[16] B Sharma and C T Sun. *LOCAL RESONANCE AND BRAGG BANDGAPS IN SANDWICH BEAMS CONTAINING PERIODICALLY INSERTED RESONATORS*. Tech. rep.

[17] Shengke Zhang et al. "Low-Frequency Bandgap Characterization of a Locally Resonant Pentagonal Phononic Crystal Beam Structure". In: *Materials* 17.7 (Apr. 2024). ISSN: 19961944. DOI: 10.3390/ma17071702.

[18] Carlos A. Galán-Pinilla et al. "Comparative Study of Dispersion Curves for LAMB Waves Using Analytical Solutions and Semi-Analytical Methods". In: *Applied Sciences (Switzerland)* 13.3 (Feb. 2023). ISSN: 20763417. DOI: 10.3390/app13031706.

[19] Michael J Vellekoop. *Acoustic wave sensors and their technology*. Tech. rep. 1998, p. 14.

[20] Junyu Zhang et al. "Acoustic Transducer and Its Applications in Biosensors". In: *Handbook of Cell Biosensors*. Springer International Publishing, 2021, pp. 1–19. DOI: 10.1007/978-3-319-47405-2{_}65-1.

[21] Abdollah Vaez Shoushtari. *SEISMIC HAZARD ASSESSMENT OF PENINSULAR MALAYSIA BASED ON NEW GROUND-MOTION PREDICTION EQUATIONS FOR SUBDUCTION EARTHQUAKES*. Feb. 2016. DOI: http://dx.doi.org/10.13140/RG.2.2.21912.85765. URL: https://www.researchgate.net/publication/327894248_SEISMIC_HAZARD_ASSESSMENT_OF_PENINSULAR_MALAYSIA_BASED_ON_NEW_GROUND-MOTION_PREDICTION_EQUATIONS_FOR_SUBDUCTION_EARTHQUAKES?channel=doi&linkId=5babbcb5a6fdccd3cb766415&showFulltext=true.

[22] C. Willberg et al. *Simulation methods for guided wave-based structural health monitoring: A review*. Jan. 2015. DOI: 10.1115/1.4029539.

[23] Mazlee Bin Mazalan et al. *Current development in interdigital transducer (IDT) surface acoustic wave devices for live cell in vitro studies: A review*. Jan. 2022. DOI: 10.3390/mi13010030.

[24] Debdyuti Mandal and Sourav Banerjee. "Surface AcousticWave (SAW) Sensors: Physics, Materials, and Applications". In: *Sensors* 22.3 (Feb. 2022). ISSN: 14248220. DOI: 10.3390/s22030820.

[25] Ranran Fang et al. "Improved two-temperature model and its application in femtosecond laser ablation of metal target". In: *Laser and Particle Beams* 28.1 (Mar. 2010), pp. 157–164. ISSN: 02630346. DOI: 10.1017/S0263034610000030.

[26] S I Anisimov et al. *Electron emission from metal surfaces exposed to ultrashort laser pulses*. Tech. rep. 1974.

[27] George D Tsibidis et al. “Damage threshold evaluation of thin metallic films exposed to femtosecond laser pulses: the role of material thickness”. In: (). DOI: `10.48550/arXiv.2205.05342`. URL: `https://www.researchgate.net/publication/360538762`.

[28] Lutz Waldecker et al. “Electron-phonon coupling and energy flow in a simple metal beyond the two-temperature approximation”. In: *Physical Review X* 6.2 (2016). ISSN: 21603308. DOI: `10.1103/PhysRevX.6.021003`.

[29] Zhibin Lin, Leonid V. Zhigilei, and Vittorio Celli. “Electron-phonon coupling and electron heat capacity of metals under conditions of strong electron-phonon nonequilibrium”. In: *Physical Review B - Condensed Matter and Materials Physics* 77.7 (Feb. 2008). ISSN: 10980121. DOI: `10.1103/PhysRevB.77.075133`.

[30] Ryan C. Ng et al. *Excitation and detection of acoustic phonons in nanoscale systems*. Sept. 2022. DOI: `10.1039/d2nr04100f`.

[31] Osamu Matsuda et al. “Fundamentals of picosecond laser ultrasonics”. In: *Ultrasonics* 56 (Feb. 2015), pp. 3–20. ISSN: 0041624X. DOI: `10.1016/j.ultras.2014.06.005`.

[32] Felix Brand and Klaus Stefan Drese. “Frequency-Resolved High-Frequency Broadband Measurement of Acoustic Longitudinal Waves by Laser-Based Excitation and Detection”. In: *Sensors* 24.5 (Mar. 2024). ISSN: 14248220. DOI: `10.3390/s24051630`.

[33] R. E. Kumon and D. C. Hurley. “Effects of residual stress on the thin-film elastic moduli calculated from surface acoustic wave spectroscopy experiments”. In: *Thin Solid Films* 484.1-2 (July 2005), pp. 251–256. ISSN: 00406090. DOI: `10.1016/j.tsf.2005.02.033`.

[34] Pascal Ruello and Vitalyi E. Gusev. “Physical mechanisms of coherent acoustic phonons generation by ultrafast laser action”. In: *Ultrasonics* 56 (Feb. 2015), pp. 21–35. ISSN: 0041624X. DOI: `10.1016/j.ultras.2014.06.004`.

[35] J. Frisch et al. “NDT of Layered Structures Using Pulse-Thermography and THz-TDS Imaging”. In: QIRT Council, July 2018. DOI: `10.21611/qirt.2018.121`.

[36] N. Chigarev, C. Rossignol, and B. Audoin. “Surface displacement measured by beam distortion detection technique: Application to picosecond ultrasonics”. In: *Review of Scientific Instruments* 77.11 (2006). ISSN: 00346748. DOI: `10.1063/1.2372739`.

[37] Kenji Katayama et al. “Generation and detection of tunable phonon polaritons using a single transmission grating”. In: *Applied Physics Letters* 92.3 (2008). ISSN: 00036951. DOI: `10.1063/1.2837617`.

[38] Zi Dong Zhang et al. “An integrable and configurable phononic beam splitter based on self-collimated surface acoustic waves”. In: *Applied Physics Express* 13.4 (Apr. 2020). ISSN: 18820786. DOI: `10.35848/1882-0786/ab7cf0`.

[39] Feng Gao et al. “On-Chip Tightly Confined Guiding and Splitting of Surface Acoustic Waves Using Line Defects in Phononic Crystals”. In: *Advanced Functional Materials* 33.14 (Apr. 2023). ISSN: 16163028. DOI: `10.1002/adfm.202213625`.

[40] Yan Feng Wang et al. “Guiding and splitting Lamb waves in coupled-resonator elastic waveguides”. In: *Composite Structures* 206 (Dec. 2018), pp. 588–593. ISSN: 02638223. DOI: `10.1016/j.compstruct.2018.08.088`.

[41] Hanqing Liu et al. “Optomechanical methodology for characterizing the thermal properties of 2D materials”. In: *APL Materials* 12.2 (Feb. 2024). ISSN: 2166532X. DOI: `10.1063/5.0190680`.

[42] AeroDiode.com. *Fiber-Coupled AOM (Acousto-Optic Modulator)*.

[43] T. Pezeril et al. “Picosecond photoexcitation of acoustic waves in locally canted gold films”. In: *Applied Physics Letters* 92.6 (2008). ISSN: 00036951. DOI: `10.1063/1.2841823`.

[44] Francesco Ruffino and Maria Grazia Grimaldi. *Nanostructuration of thin metal films by pulsed laser irradiations: A review*. Aug. 2019. DOI: `10.3390/nano9081133`.

[45] A. I. Kuznetsov, J. Koch, and B. N. Chichkov. “Nanostructuring of thin gold films by femtosecond lasers”. In: *Applied Physics A: Materials Science and Processing* 94.2 (Feb. 2009), pp. 221–230. ISSN: 09478396. DOI: `10.1007/s00339-008-4859-6`.

# Appendix A

## Appendix A1: Python Code for Plotting Time-signal, FFT, 2 ns Zoom-in Time-signal, FFT of 2 ns Zoom-in of 4 measurements.

```
# Loading the measurement files
index = 9                                  #Change which file from folder is displayed
tempData = data[folder][keys[index]]
time, baseSignal_raw1 = GetMeasurementData(tempData)

index = 10                                 #Change which file from folder is displayed
tempData = data[folder][keys[index]]
time, baseSignal_raw2 = GetMeasurementData(tempData)

index = 11                                  #Change which file from folder is displayed
tempData = data[folder][keys[index]]
time, baseSignal_raw3 = GetMeasurementData(tempData)

index = 12                                  #Change which file from folder is displayed
tempData = data[folder][keys[index]]
time, baseSignal_raw4 = GetMeasurementData(tempData)


time = np.linspace(0, 20, 1024 * 6)  # Simulating time from 0 to 20 ns in 6 windows


# Sampling parameters
T = 20e-9  # Total signal duration
N = 6144  # Number of samples
dt = T / N  # Time step
fs = 1 / dt  # Sampling frequency
f_nyquist = fs / 2  # Nyquist frequency


# Compute FFT of both signals
fft_signal1 = np.fft.fft(baseSignal_raw1)
fft_signal2 = np.fft.fft(baseSignal_raw2)
fft_signal3 = np.fft.fft(baseSignal_raw3)
fft_signal4 = np.fft.fft(baseSignal_raw4)
freqs = np.fft.fftfreq(N, d=dt)  # Frequency axis
fft_magnitude1 = np.abs(fft_signal1)
fft_magnitude2 = np.abs(fft_signal2)
fft_magnitude3 = np.abs(fft_signal3)
fft_magnitude4 = np.abs(fft_signal4)


# Filter positive frequencies only
positive_freqs = freqs[:N//2]
positive_magnitude1 = fft_magnitude1[:N//2]
positive_magnitude2 = fft_magnitude2[:N//2]
positive_magnitude3 = fft_magnitude3[:N//2]
positive_magnitude4 = fft_magnitude4[:N//2]


# Select only the range 50 MHz to 200 GHz
f_min, f_max = 50e6, 200e9  # 50 MHz to 200 GHz
mask = (positive_freqs >= f_min) & (positive_freqs <= f_max)

Label1 = 'd=20$\mu$m'
Label2 = 'd=45$\mu$m'
Label3 = 'd=75$\mu$m'
Label4 = 'PnC'
```

```
#Plot Full Time-Domain Signals
plt.figure(figsize=(10, 4))
plt.plot(time, baseSignal_raw1, color='b', label=Label1)
plt.plot(time, baseSignal_raw2, color='r', label=Label2)
plt.plot(time, baseSignal_raw3, color='g', label=Label3)
plt.plot(time, baseSignal_raw4, color='k', label=Label4)
plt.xlabel('Time (ns)')
plt.ylabel("Amplitude")
plt.title('Time-Domain Signals')
plt.legend()
plt.grid()
plt.show()


#Plot FFT
plt.figure(figsize=(10, 5))
plt.loglog(positive_freqs[mask], positive_magnitude1[mask], color='b', label=Label1)
plt.loglog(positive_freqs[mask], positive_magnitude2[mask], color='r', label=Label2)
plt.loglog(positive_freqs[mask], positive_magnitude3[mask], color='g', label=Label3)
plt.loglog(positive_freqs[mask], positive_magnitude4[mask], color='k', label=Label4)
plt.xlabel('Frequency (Hz)')
plt.ylabel('Magnitude')
plt.title('FFT')
plt.legend()
plt.grid(which='both', linestyle='--', linewidth=0.5)
plt.show()


#ADDITIONAL PLOTS FOR FIRST 2 ns


# Extract first 2 ns of the signals
time_2ns_mask = time <= 1
time_2ns = time[time_2ns_mask]
signal_2ns1 = baseSignal_raw1[:len(time_2ns)]
signal_2ns2 = baseSignal_raw2[:len(time_2ns)]
signal_2ns3 = baseSignal_raw3[:len(time_2ns)]
signal_2ns4 = baseSignal_raw4[:len(time_2ns)]


# FFT of first 2 ns of both signals
N_2ns = len(signal_2ns1)
fft_signal_2ns1 = np.fft.fft(signal_2ns1)
fft_signal_2ns2 = np.fft.fft(signal_2ns2)
fft_signal_2ns3 = np.fft.fft(signal_2ns3)
fft_signal_2ns4 = np.fft.fft(signal_2ns4)
freqs_2ns = np.fft.fftfreq(N_2ns, d=dt)
fft_magnitude_2ns1 = np.abs(fft_signal_2ns1)
fft_magnitude_2ns2 = np.abs(fft_signal_2ns2)
fft_magnitude_2ns3 = np.abs(fft_signal_2ns3)
fft_magnitude_2ns4 = np.abs(fft_signal_2ns4)


# Filter positive frequencies
positive_freqs_2ns = freqs_2ns[:N_2ns//2]
positive_magnitude_2ns1 = fft_magnitude_2ns1[:N_2ns//2]
positive_magnitude_2ns2 = fft_magnitude_2ns2[:N_2ns//2]
positive_magnitude_2ns3 = fft_magnitude_2ns3[:N_2ns//2]
positive_magnitude_2ns4 = fft_magnitude_2ns4[:N_2ns//2]


#Plot Time-Domain Signals for First 2 ns
plt.figure(figsize=(10, 4))
```

```
plt.plot(time_2ns, signal_2ns1, color='b', label=Label1)
plt.plot(time_2ns, signal_2ns2, color='r', label=Label2)
plt.plot(time_2ns, signal_2ns3, color='g', label=Label3)
plt.plot(time_2ns, signal_2ns4, color='k', label=Label4)
plt.xlabel('Time (ns)')
plt.ylabel('Amplitude')
plt.title('Time-Domain Signals (First 2 ns)')
plt.legend()
plt.grid()
plt.show()


#Plot FFT of First 2 ns
plt.figure(figsize=(10, 5))
plt.loglog(positive_freqs_2ns, positive_magnitude_2ns1, color='b', label=Label1)
plt.loglog(positive_freqs_2ns, positive_magnitude_2ns2, color='r', label=Label2)
plt.loglog(positive_freqs_2ns, positive_magnitude_2ns3, color='g', label=Label3)
plt.loglog(positive_freqs_2ns, positive_magnitude_2ns4, color='k', label=Label4)
plt.xlabel('Frequency (Hz)')
plt.ylabel('Magnitude')
plt.title('FFT (First 2 ns)')
plt.legend()
plt.grid(which='both', linestyle='--', linewidth=0.5)
plt.show()
```

## Appendix A2: Python Code for Plotting COMSOL simulation data.

```
#Load COMSOL Data
comsol_data = pd.read_csv("FileName.csv", header=None)
eigen_freqs = comsol_data[0].values * 1e9  #Convert MHz to Hz
eigen_disp = comsol_data[1].values * 1e-2   #Apply magnitude shifting

#Plot COMSOL Data
plt.figure(figsize=(10, 5))
plt.loglog(eigen_freqs, eigen_disp, 'k', linewidth = 1, markersize=2)

plt.xlabel('Frequency (Hz)')
plt.ylabel('Magnitude')
plt.title('FileTitle')
plt.grid(which='both', linestyle='-', linewidth=0.1)
plt.xlim(0.8e8, 100e9)
plt.ylim(1e-5, 3e-1)
plt.show()
```